INVESTIGATION OF BEAMING LIGHT THROUGH NANOAPERTURES USING REAL METALS FOR APERTURE BASED IMAGING DEVICES

by

Jimmy N. B. Koo
Bachelor of Applied Science, University of British Columbia, 2005

THESIS SUBMITTED IN PARTIAL FULFILLMENT OF
THE REQUIREMENTS FOR THE DEGREE OF

MASTER OF APPLIED SCIENCE

In the
School of Engineering Science

SIMON FRASER UNIVERSITY

Spring 2011

APPROVAL

Name: **Jimmy N. B. Koo**

Degree: **Master of Applied Science**

Title of Thesis: **Investigation of Beaming Light through Nanoapertures Using Real Metals for Aperture Based Imaging Devices**

Examining Committee:

Chair: **Dr. John Jones, P. Eng**
Associate Professor

_____

Dr. Marinko Sarunic, P. Eng
Senior Supervisor
Assistant Professor

_____

Dr. Ash Parameswaran, P. Eng
Supervisor
Professor

_____

Dr. Andrew Rawicz, P. Eng
Internal Examiner
Professor

Date Defended/Approved: 13 April 2011

Declaration of
Partial Copyright Licence

ABSTRACT

We investigated light beaming through nanoapertures surrounded by periodic corrugations as a technology for aperture based imaging. Using the Finite-Difference Time-Domain (FDTD) method, we performed simulations of nanoapertures in Perfect Electric Conductor (PEC), gold, and silver to predict the beam profile when varying the geometric parameters of the corrugations. We found that the results of the FDTD simulations for nanoapertures in PEC resembled those from the perfect conductor model presented in the literature, but the FDTD simulations using silver and gold did not predict beam formation. We fabricated nanoapertures surrounded by corrugations in silver films, and measured the beam profiles with knife-edge experiments. The measured beam profiles were narrower than predicted by the FDTD simulations, and there was no appreciable difference observed in the light transmitted through a nanoaperture with or without corrugations. The results suggest PEC is a poor approximation for real metals in surface plasmon assisted beaming applications.

Keywords: nanoaperture, surface plasmon, finite-difference time-domain

Subject Terms: Aperture Based Imaging, Biomedical Optics

ACKNOWLEDGEMENTS

First and foremost I would like to thank my supervising committee for their guidance and support during my research. My senior supervisor, Dr. Marinko Sarunic, made this project possible. I am indebted to him for his time and patience he spent helping me. Dr. Ash Parameswaran and Dr. Andrew Rawicz gave much advice that was appreciated. Thank you to Dr. John Jones for graciously chairing my thesis defence.

Much appreciation goes to Dr. Karen Kavanagh for allowing me to use the facilities at 4D labs at SFU for fabricating the nanoapertures. Li Yang spent much of her time teaching me how to use the equipment and I am very grateful of her help.

I would like to thank Dr. Todd Simpson at the nanofabrication facility at UWO for making the nanoapertures for this project.

I would also like to express my gratitude to everyone in my research group for their support in both intellect and morale. Without their help the journey would have been a lot tougher.

I would finally like to express my heart-felt thanks to my family and friends. Your kind words got me through the rough times and your encouragements allowed me succeed.

TABLE OF CONTENTS

LIST OF FIGURES

LIST OF TABLES

GLOSSARY

ABID	Aperture Based Imaging Devices
MEMS	Micro-Electrical Mechanical Systems
NSOM or SNOM	Near-field Scanning (or Scanning Near-field) Optical Microscopy
PEC	Perfect Electrical Conductor
PCM	Perfect Conductor Model
QPCM	Quasi-Perfect Conductor Model
SP	Surface Plasmon
FDTD	Finite-Difference Time-Domain
FIB	Focused Ion Beam
SEM	Scanning Electron Microscope
SFU	Simon Fraser University
UWO	University of Western Ontario
Nd:YAG	Neodymium-doped Yttrium Aluminum Garnet
CCD	Charge-coupled Device
erf	Error function
FWHM	Full-width Half-max

1 INTRODUCTION

1.1 Motivation

The optical microscope allows us to see enlarged images of microscopic objects. The world of microbiology was opened for exploration when Leeuwenhoek looked through his optical microscope and saw single cell organisms for the first time. Since then, many different ways have been invented to create magnified images. However, the operation of an optical microscope has mostly remained the same, relying on lenses and mirrors to collect light. These components define the large physical dimensions of the optical microscope that have confined it to the laboratory [1][2].

Similar to how the microchip transformed the computer from a room-sized research equipment to a consumer device in everyone's home, optical micro-devices are being developed to transform the optical microscope out of the laboratory to a convenient and portable device that can be used in the field. The ultimate goal is to allow scientists, doctors, and researchers to see the microscopic samples in the field instead of having to wait until the sample is sent to a laboratory for analysis.

The emerging field of Aperture-Based Imaging Devices (ABIDs) aims to reduce the size and complexity of optical microscopes. The goal is to fabricate these

devices on Micro-Electrical Mechanical Systems (MEMS). The motivation for developing such a device is to create an imaging modality that has advantages in portability and complexity over established imaging technologies (such as traditional optical microscopy and near-field scanning microscopy (NSOM)). The purpose of this thesis is to extend the experimental and theoretical analysis of aperture based imaging which may lead to miniaturizable optical systems.

1.2 Overview of Current Microscopy Techniques

Traditional optical microscopy forms an image by focusing light scattered from a sample on a plane using lenses and mirrors. The ability of a microscope to discern detail is determined by its resolving power, defined as the minimum distance between two nearby points that the system is able to differentiate. For optical microscopy, the numerical aperture of the system and the diffraction of light passing through the finite apertures of the lenses limit the resolving power. For light arising from a point source passing through the circular aperture of a lens, the diffraction pattern projected onto the image plane resembles concentric rings of alternating bright and dark intensity in what is known as an Airy pattern. Lord Raleigh established the criterion for the resolving limit of an optical system; the resolution limit is the distance at which the maximum of the diffraction pattern of one source coincides with the first minimum of the diffraction pattern of the other [3]. The angular resolution, θ, is given as

$$\sin\theta = 1.220\frac{\lambda}{D}$$ [3], Eq. 1-1

where λ is the imaging wavelength, and D is the diameter of the lens. Then for the human eye looking through a standard compound light microscope, the resolving power is

$$R = \frac{1.220\lambda}{NA_{condenser} + NA_{objective}}, \qquad \text{Eq. 1-2}$$

where R is the minimum resolvable distance, $NA_{condenser}$ is the numerical aperture of the condenser, $NA_{objective}$ is the numerical aperture of the objective lens. From a practical standpoint, NA is limited to about 1.40 for the best oil immersion lens. Using the blue visible light for illumination, λ=450nm, Equation 1-2 gives the approximate resolution of optical microscopes of about 200nm. For imaging below this resolution limit, a different technique must be used to bypass the effects of diffraction.

1.2.1 Near-field Scanning Microscopy

Near-field Scanning Optical Microscopy (NSOM), alternatively called Scanning Near-field Optical Microscopy (SNOM), is a high-resolution imaging technique that overcomes the diffraction limit in traditional lens-based optical microscopy [4]. NSOM works by placing an optical probe very close to the sample (<100nm), and can either illuminate or collect light from a very small area of the sample. The probe is physically raster scanned across the sample to form a two-dimensional image. The resolution (spot size) is determined not only by the size of the probe tip, but also by the distance between the probe tip and the sample. The probe tip,

which can be made from a pulled fibre or milled structure by focused ion beam, can be as small as 20nm [5]. To maintain a constant distance between the probe and the sample, a vibrating tuning fork is mounted beside the probe tip. As the fork approaches the sample, shear forces increase due to Van de Waal forces that dampen the vibration and change the resonant frequency. The probe distance to the sample is kept fixed by maintaining a constant vibration frequency. Intensity variation at the detector is recorded as the position of the probe tip is scanned across the surface of the sample.

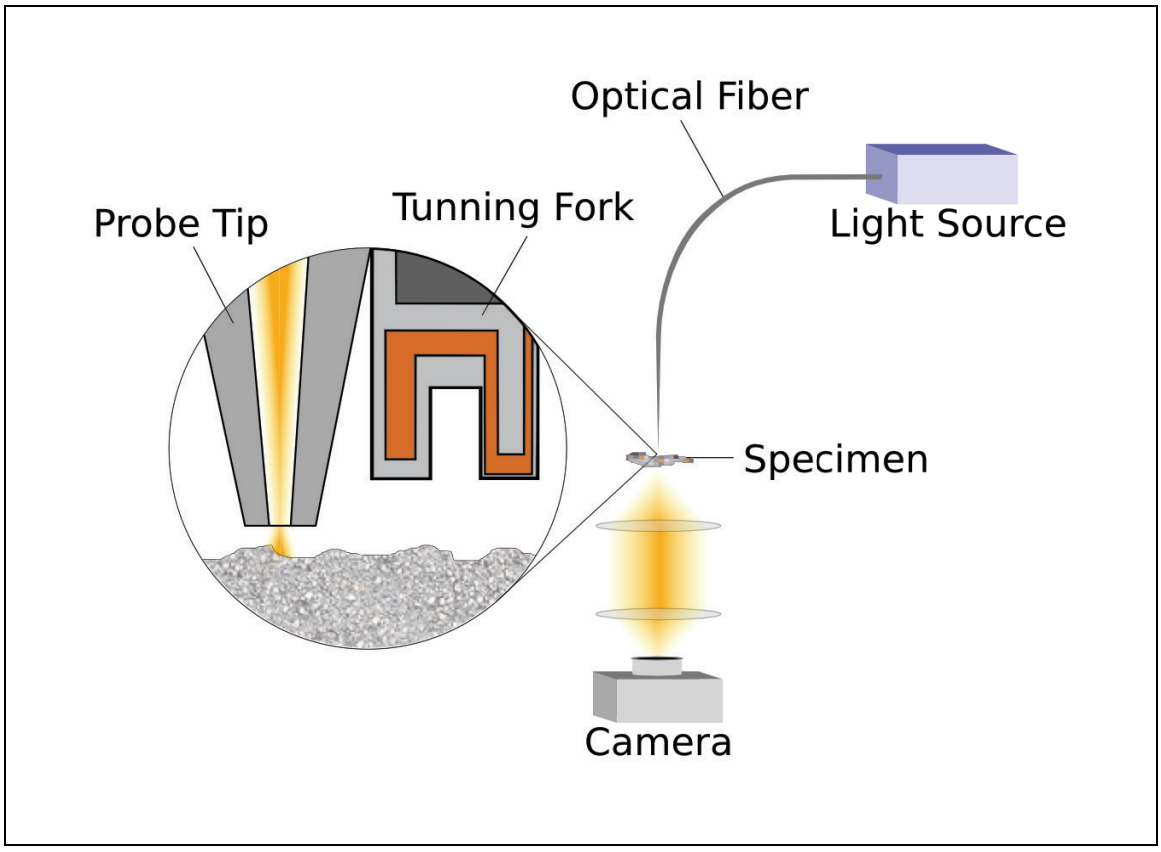

Figure 1-1: NSOM

1.2.1.1 Aperture Based Imaging Devices

Both imaging techniques discussed in previous sections are large and bulky, and the investigation of alternatives for microscopic imaging which can be miniaturized is an active area of research. An exciting emerging research area for high-resolution imaging concentrates on the use of an aperture to limit the region of a sample being imaged. The basic imaging principle of a so called Aperture Based Imaging Device (ABID) is conceptually similar to near-field scanning optical microscopy (NSOM). In an ABID, the light is spatially filtered through an aperture in an opaque surface. As in NSOM, a two dimensional image is acquired by the shifting of the aperture relative to the sample. To achieve resolution comparable to the optical microscope, the diameter of the aperture must be on the order of the wavelength of light or smaller. Compared to NSOM, ABIDs can be implemented without the precision distance control system between the sample and the probing tip, giving ABIDs robustness for implementation outside laboratory conditions. The compromise of reduced sample working distance control is lower resolution, making the imaging ability of ABID closer to that of a standard microscope than NSOM. The potential ability to implement ABID on MEMS has the promise of offering an inexpensive microscopy modality alternative to optical microscopes.

Heng et al. first demonstrated ABID with their opto-fluidic microscope [6]. An array of subwavelength-sized apertures was used to collect light that interacted with specimen flowing through a microfluidic channel. The resolving power of this device depended on the size of the aperture and the distance from the specimen

to the apertures. For high-resolution imaging (~1μm laterally), it was required that the specimen remain very close to the apertures (<1μm). Heng et al. classified their system, which used the aperture as the collector, as a type-II ABID device [7].

A type-I ABID device was defined with light travelling in the reverse direction; light from the aperture passes through the specimen and is collected by a photo-detector [7]. The benefit of the type-I ABID is that much higher light collection efficiency can be obtained over type-II ABID systems. This is important for application such as fluorescence where the light intensity can be very low (on the order of nanoWatts). The resolving power of such a type-I ABID device is determined by the spot size of the optical beam incident on the specimen. Therefore, the specimen can be placed at any distance from the aperture plane as long as the desired spot size can be formed at that distance. In the macro world, the spot would be formed using a glass lens, but that is not readily compatible with MEMS-based lab-on-a-chip systems. An alternative to lenses is to use diffractive optics.

High-resolution imaging with type-I ABID systems requires the use of small diameter apertures, which will introduce diffraction as schematically illustrated in Figure 1-2. In order to get higher resolution, the aperture must be made smaller. As the dimension of the aperture approaches the wavelength of light, it will be diffracted in all angles and is not useful for imaging. Based on a novel research direction pioneered by Lezec at al. [8], the angular distribution of light transmitted

through a subwavelength aperture can be controlled. In Lezec's technique, the subwavelength aperture is bored on a thin metal surface. The evanescent waves on the metal surface can be recoupled back into free-space by introducing periodic corrugations around the aperture. The collective light emerging from the aperture and corrugation interfere to shape the transmitted light into a well defined beam.

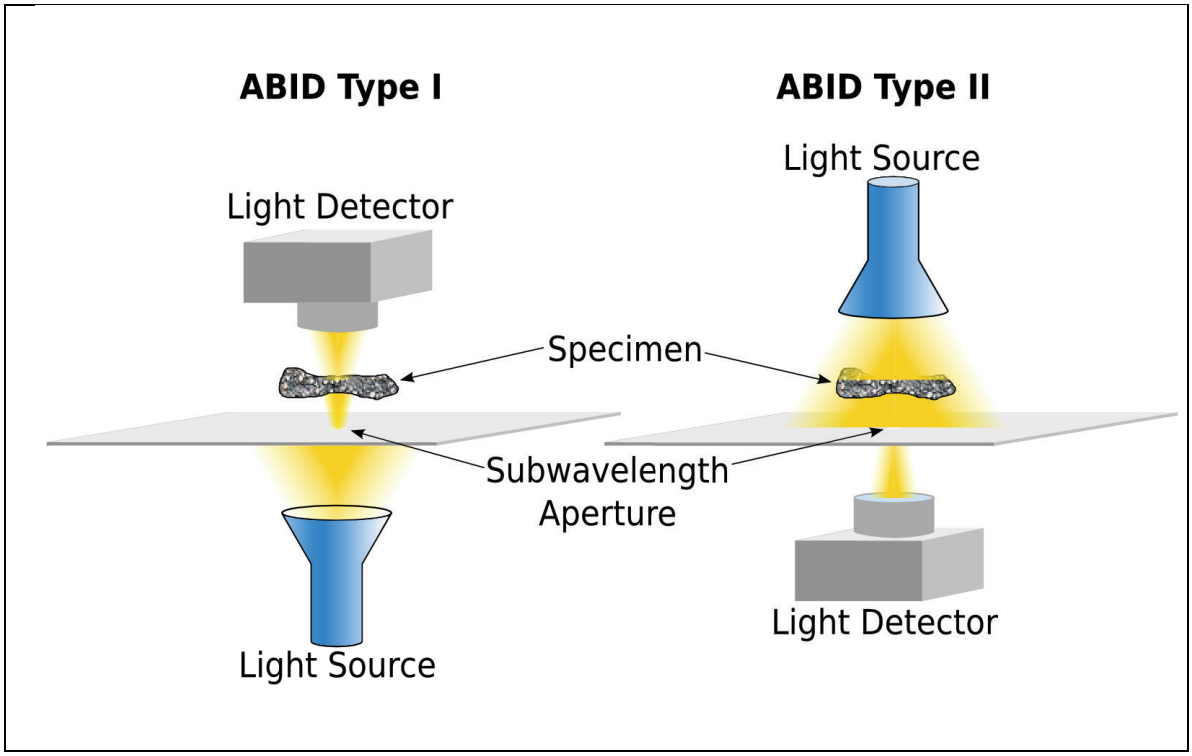

Figure 1-2: The two types of Aperture Based Imaging Devices

1.2.2 Beaming light from a Subwavelength Aperture with Periodic Corrugations

An analytical mathematical model was developed to explore the geometric parameters that would confine light to a narrow beam [9]. Calculations from this model suggested beaming can be achieved at distances beyond the near-field

regime [10], allowing the development of type-I ABID systems. The Martin-Moreno model assumes that a Perfect Electrical Conductor (PEC) is a good approximation for real metals like silver and gold [9].

Wang et al. [11] proposed a modification to Lezec's analytical model that accounts for the field penetration into real metals. This field penetration takes into account that electromagnetic waves are not completely extinct at the air-to-metal boundary. The model proposed by Wang is thus referred to as Quasi-Perfect Conductor Model (QPCM), to distinguish it from Martin-Moreno's model, referred to as the Perfect Conductor Model (PCM). The main contribution of the QPCM is that it adds a phase term that affects the field admittance at the corrugations. While the PCM model has been matched by some experimental results, the QPCM has not been verified with experimental results but has been investigated with computer simulations.

1.3 Objective

The purpose of this thesis is to build on the initial investigations of beaming light through nanoapertures. We want to compare the results from QPCM and PCM. We will do this in simulation using the Finite-Difference Time-Domain (FDTD) technique. The simulations will be run on perfect conductors, as well as on real metals such as gold and silver which approximate perfect conductors. The FDTD results will be compared to the results in the literature. The design that will be investigated is the bull's eye corrugations proposed by Lezec for creating a beam of circular cross section. We will use the simulation tools to investigate the

performance sensitivity of the design including corrugation depth, corrugation period, corrugation width, and number of corrugations.

Next, we will complement the simulations with experimental measurements. The design analysis performed in the previous step will be used to help us determine the ideal geometric parameters for fabrication. For the targeted application of a type-I ABID, the important parameters are beam shape: spot size and divergence. These will be investigated on the fabricated devices using a knife-edge measurement to measure the beam width.

The results from the simulations and experiments will contribute to our knowledge of generating beaming light through nanoapertures, and address issues of fabricating designs when working with real metals (quasi-perfect conductors). The contributions of this thesis are both in terms of simulations and experiment.

1.4 Summary

Current optical microscopy techniques have drawbacks that limit their usage in certain areas. Their size and complexity prevents them from being used out in the field. Near-field scanning microscopy provides high-resolution in the nanometres but their usage is limited to within the laboratory. Aperture Based Imaging Devices have the potential to challenge NSOM for its resolving power while reducing in complexity and increasing flexibility. This thesis will investigate

the type-I ABID comprised of a nanoaperture surrounded by periodic corrugations.

In chapter 2, we will start with a review of the theoretical basis for the formation of surface plasmon polaritons. It will be followed by a description of the analytical model of light beaming through a subwavelength aperture developed by Martin-Moreno. This model was refined by Wang, taking into account the attenuating properties of real metals. This chapter will end with a discussion of the finite-difference time-domain method for simulation electromagnetic waves and near-to-far-field transformation for obtaining scattered radiation in the far-field.

Chapter 3 will use the mathematical tools described at the end of chapter 2 to simulate light beaming through a subwavelength aperture with surrounding periodic corrugations developed by Martin-Moreno. Several physical parameters of the corrugations were varied to investigate their effects on light beaming: number of corrugation, corrugation period, corrugation depth, and corrugation width. These simulations were carried out with PEC as the barrier material, as well as real conductors gold and silver.

Chapter 4 will describe the fabrication procedure of a subwavelength aperture with surrounding periodic corrugations. A description of the deposition of the barrier metallic film and the milling of the aperture and corrugations will be provided.

The characterization of the subwavelength aperture will be discussed in chapter 5. It will consist of a beam profile measurement using a knife-edge type experiment.

In chapter 6, we will compare the results from our simulations with those published in the literature. We will also discuss the experimental results and compare them to our FDTD simulations.

We will conclude this thesis in chapter 7 and discuss some of the future work that can further the investigation of nanoaperture with corrugations in metal for high-resolution nanoaperture microscopy.

2 BEAM SHAPING LIGHT TRANSMITTED THROUGH NANOAPERTURES

The wave nature of light is responsible for diffraction at the edge of objects in its path. Light travelling through apertures diffracts more strongly as the diameter of the aperture is reduced closer to the wavelength. Diffraction of light from subwavelength apertures is anticipated to result in highly divergent light, similar to light being re-radiated from a single point. However, the transmitted light can be shaped into a beam by interaction of the radiant field with free electric charges called surface plasmons. In this chapter, the theory behind beaming light through subwavelength apertures by interaction with surface plasmons is introduced. Additionally, the concepts behind finite element modelling for computational simulation of electromagnetic waves interacting with subwavelength apertures are introduced. Computer simulations of surface plasmons enhanced transmission of light through nanoaperture structures will be presented in the next chapter.

2.1 Theory of Light Beaming through Subwavelength Apertures in Perfectly Conducting Surfaces

2.1.1 Surface Plasmons

A surface plasmon (SP), or formally surface plasmon polaritons are electromagnetic waves trapped on the surface of metals due to interactions with the free electrons [12]. They are generated when photons impinge on the surface

of metals. For a given frequency ω, the photon momentum $p_o=\hbar k_o$ is less than the surface plasmon momentum $p_{sp}=\hbar k_{sp}$, where

$$k_{sp} = \frac{\omega}{c}\sqrt{\frac{\varepsilon_m \varepsilon_d}{\varepsilon_m + \varepsilon_d}} \text{ [12],} \qquad \text{Eq. 2-1}$$

and ε_m is the permittivity of the metal, and ε_d is the permittivity of the surrounding dielectric. In order for surface plasmons to form, the difference in momentum between the photons and the surface plasmons must be accounted for. This can be achieved by increasing the incident momentum through prism coupling (Kretschman configuration) [13], or by scattering the light from defects in the surface of the metal, such as bumps or holes.

The propagation behaviours of the surface plasmons are different in the plane of the metal than in the direction perpendicular to the surface. The field component perpendicular to the surface decays exponentially with distance; therefore, power does not dissipate from the surface and is not lost to free space unless the surface plasmons encounter a defect. Because they are trapped on the metal, the surface plasmons are considered evanescent waves. Unlike electromagnetic waves in a vacuum, surface plasmons decay as they travel across the surface of the metal. The distance for which the surface plasmons propagate is determined by the absorption of the metal and the refractive index of the surrounding dielectric. Similar to skin depth, the distance at which the surface plasmons attenuate to 1/e of its initial amplitude is given by

$$L = \frac{1}{2\tilde{k}_{sp}} \text{ [12]}, \qquad \text{Eq. 2-2}$$

where $\tilde{k}_{sp}$ is the imaginary part of the surface plasmon wave vector. This is important because it determines the localized range at which optical designs with surface plasmons are applicable.

Surface plasmons can be recoupled back into electromagnetic waves in free space if they encounter defects as they propagate along the surface. Due to the wave vector relationship discussed above, the re-radiated energy can interfere with the EM field that created the surface plasmons. Careful design of defects on the surface of the metal, such as geometric patterns of corrugations, can be used to engineer constructive or destructive interference. A particular area where this is of interest is light transmission through subwavelength apertures. Surface plasmons have been used for enhanced transmissions by designing surface corrugations on the incident side of the metal [14]. Additionally, the corrugations can be on the exit surface, and in this scenario, the constructive and destructive interference can be engineered for highly directional beaming. This approach was developed by Martin-Moreno [9] to create beaming light and is discussed in the next section.

2.1.2 Beaming Light through a Subwavelength Aperture

A model for the interaction of light with a subwavelength aperture with periodic corrugation was developed by Martin-Moreno et al. [9]. Energy re-radiated into

free space from the surface plasmons interaction with the corrugation was used to shape the diverging light into a beam. The circular symmetry of a “bull’s eye” pattern of concentric rings surrounding the aperture is illustrated in Figure 2-1. The rings are only corrugations in the surface of the metal, and do not extend through the full thickness of the material.

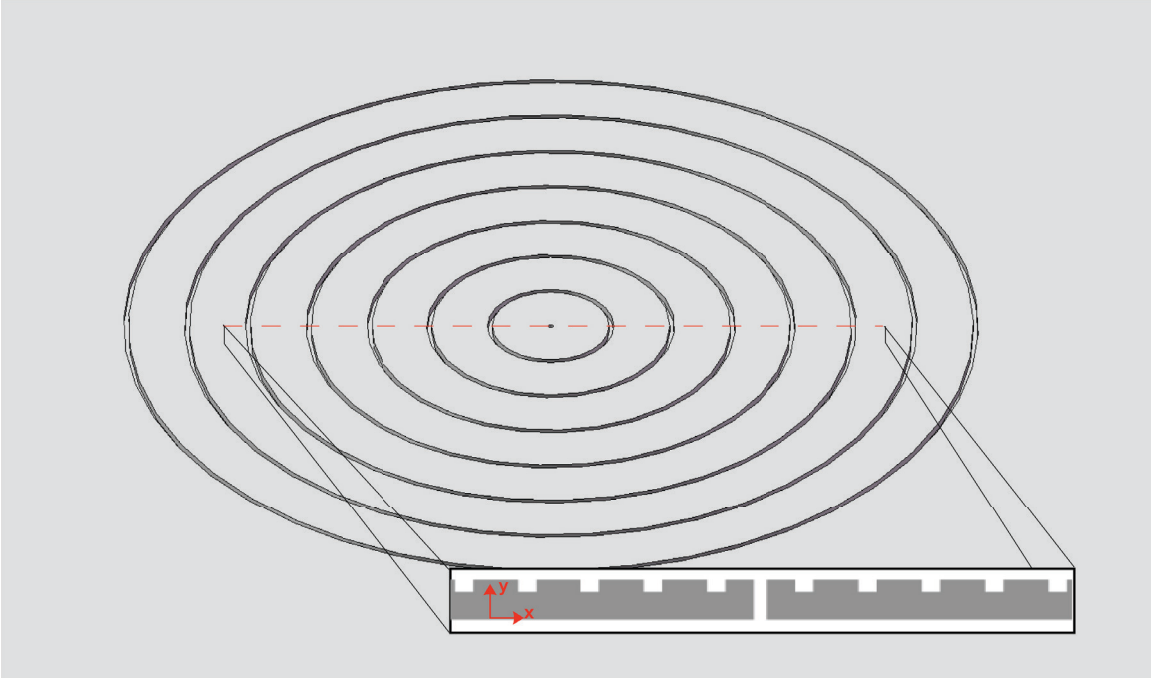

Figure 2-1: Representative bull’s eye pattern of periodic concentric ring corrugations surrounding the central nanoaperture.

Light at the exit of the nanoaperture excite surface plasmons at the edge of the nanoaperture. Surface plasmons then propagate away from the nanoaperture along the surface until they encounter the periodic corrugations. At each corrugation, some of the surface plasmon energy gets re-radiated into free space while the remaining energy continues as surface plasmons and propagates to other corrugations.

In Martin-Moreno's [9] description of the surface plasmon interaction with the corrugations, they only considered the fundamental mode of plasmonic oscillations and assumed that the barrier material was a perfect electrical conductor. The fraction of the electric field emanated by corrugation β that reaches α is given by $G_{\alpha\beta}$,

$$G_{\alpha\beta} = \frac{ik}{2}\iint \phi_\alpha^*(x)\phi_\beta(x')H_0^{(1)}(k|x-x'|)dxdx' \text{ [9]}, \qquad \text{Eq. 2-3}$$

where $k = 2\pi/\lambda$ (λ is the wavelength inside the aperture); $\phi_\alpha = 1/\sqrt{a}$ at corrugation α and 0 otherwise; and $H_0^{(1)}$ is the zeroth order Hankel function of the first kind. The electric field at a particular corrugation α is the sum of the electric fields that reach it from other corrugations. The electric field emanating from the aperture is the sum of the electric field from the corrugation plus the field inside the aperture. Admittance (inverse of impedance) is the frequency dependent factor that determines how well surface plasmons travel from one corrugation to another. For the corrugation, the admittance is $Y_\alpha = \cot(kh)$, and for the aperture $Y_0 = -i$. Using this, Martin-Moreno created a set of linear equations for the EM field coupled into free space at each corrugation, E_α:

$$\sum_\beta G_{\alpha\beta}E_\beta = Y_\alpha E_\alpha \quad (\alpha \neq 0) \text{ [9]}. \qquad \text{Eq. 2-4}$$

The EM field emerging from the aperture is given by E_0,

$$\sum_{\beta} G_{0\beta} E_{\beta} = 2iA_0 + Y_0 E_0 \text{ [9]},$$ Eq. 2-5

where A_0 is the electric field inside the aperture before leaving the opening.

Equations 2-4 and 2-5 describe the amplitude of a point source EM field at the corrugations due to the surface plasmons. The frequency of the radiation is the same as the incident light, and the light from the corrugations and the central aperture can interfere. Martin-Moreno developed the equations to calculate the interference pattern for light transmitted through the aperture and interfering with the re-emitted light from the corrugations. The magnetic field of the light in the free space at a distance r from the aperture at polar angle θ is described by:

$$H_y(r,\theta) = \frac{1}{\mu_o c} \sum_{\alpha=-N}^{\alpha=N} E_\alpha G_\alpha(r,\theta) \text{ [9]},$$ Eq. 2-6

where

$$G_\alpha(r,\theta) = \frac{ik}{2} \int \phi_\alpha^*(x) H_0^{(1)}(k|x\vec{u}_x - \vec{r}|) dx \text{ [9]}.$$ Eq. 2-7

2.1.3 Quasi-Perfect Conductor Model

The analysis by Martin-Moreno was based on the assumption that the aperture and the corrugations were fabricated in a perfect electrical conductor. Wang et al. proposed a refined model for light emanating from a subwavelength aperture with periodic corrugations in a real metal [11]. Instead of assuming a perfect electrical

conductor (where the electric field is zero), the model takes into account the small penetration of electric field into the metal permitted by finite conductivity. This modification changes the admittance at the corrugation opening. The admittance becomes

$$Y_\alpha = \frac{k}{\eta}\cot(\eta h + \varphi) \text{ [11]}, \qquad \text{Eq. 2-8}$$

where

$$\varphi = \frac{1}{2}\arg\left(\frac{\varepsilon_m^{1/2} - 1}{\varepsilon_m^{1/2} + 1}\right) \text{ [11]}, \qquad \text{Eq. 2-9}$$

and η is determined by the following relation:

$$\tanh(\sqrt{\eta^2 - k^2}\,a) = \frac{\sqrt{\eta^2 - \varepsilon_m k^2}}{\varepsilon_m \sqrt{\eta^2 - k^2}} \text{ [11]}, \qquad \text{Eq. 2-10}$$

and ε_m is the relative permittivity which can be calculated by the Drude relation

$$\varepsilon_m = \varepsilon_\infty - \frac{\omega_p^2}{\omega(\omega + i\kappa)} \text{ [11]}. \qquad \text{Eq. 2-11}$$

ε_∞ is the relative permittivity at frequencies that are high but below interband transition energy; ω_p is the plasma frequency of the metal; and κ is the absorption frequency.

The additional phase term in Equation 2-8 introduced by Wang et al. [11] indicated that the recoupled light from the corrugations is dependent on the material properties of the metal. As such, we can expect the propagation pattern from a nanoaperture with surrounding corrugations in metals to differ from the PEC model. In order to investigate this, we will use computer based simulations using the finite-difference time-domain method.

2.2 Finite-Difference Time-Domain

Computer based simulations were used to investigate the beaming of light through a nanoaperture in both perfect electrical conductor and real metals. The software tool used for this is a finite element program called Lumerical. Prior to discussing the results of the simulations in Chapter 3, the operation of Lumerical as a Finite-Difference Time-Domain (FDTD) is described.

Finite-Difference Time-Domain is a mesh-based computational modelling method for approximating differential equations. It is commonly used for modelling electromagnetic waves. The computation method can be described by the following. First, the simulation domain is discretized with a mesh. The initial electric and magnetic field vectors are provided for each mesh element. The differential forms of Maxwell's equation are approximated using finite difference equations. These equations are then used to calculate the electric and magnetic fields in discrete time steps throughout the simulation domain.

The mesh is aligned to the Cartesian coordinates. It is generated based on the requirements of the simulation domain and the wavelength of the electromagnetic wave in question. The size of each mesh cell can be constant or variable throughout the simulation domain. Clearly, the size of a cell must be several factors smaller than the spatial feature that it is discretizing, otherwise the feature would be invisible to the mesh. The cell size also must be much smaller than the wavelength of interest, as cells of approximately equal or larger size would cause unstable behaviour in the simulation [15].

2.2.1 Yee Cell

A standard technique for placing the electric and magnetic fields is referred to as the Yee Cell, shown in Figure 2-2 [15]. The electric field vectors are stored parallel to the cell edges while magnetic field vectors are stored perpendicular to cell faces. The differential forms of Maxwell's equations are used for the computation [16]. The time derivatives of the curl equations,

$$\nabla \times E = -\frac{\partial B}{\partial t} \text{ [17]}, \qquad \text{Eq. 2-12}$$

$$\nabla \times B = \mu_{\circ}\varepsilon_{\circ}\frac{\partial E}{\partial t} \text{ [17]}, \qquad \text{Eq. 2-13}$$

are discretized using central difference equations. The simulation is propagated forwards in time while the electric and magnetic field information are stored in spatial coordinates. For each time step, the electric and magnetic field are

calculated alternately. Specifically, the electric fields throughout the simulation domain are calculated using the finite difference approximation of the curl of the magnetic field in one time step. Then the magnetic fields are calculated using the finite difference approximation of the curl of the electric field in the next time step. This process is repeated until the desired time has elapsed.

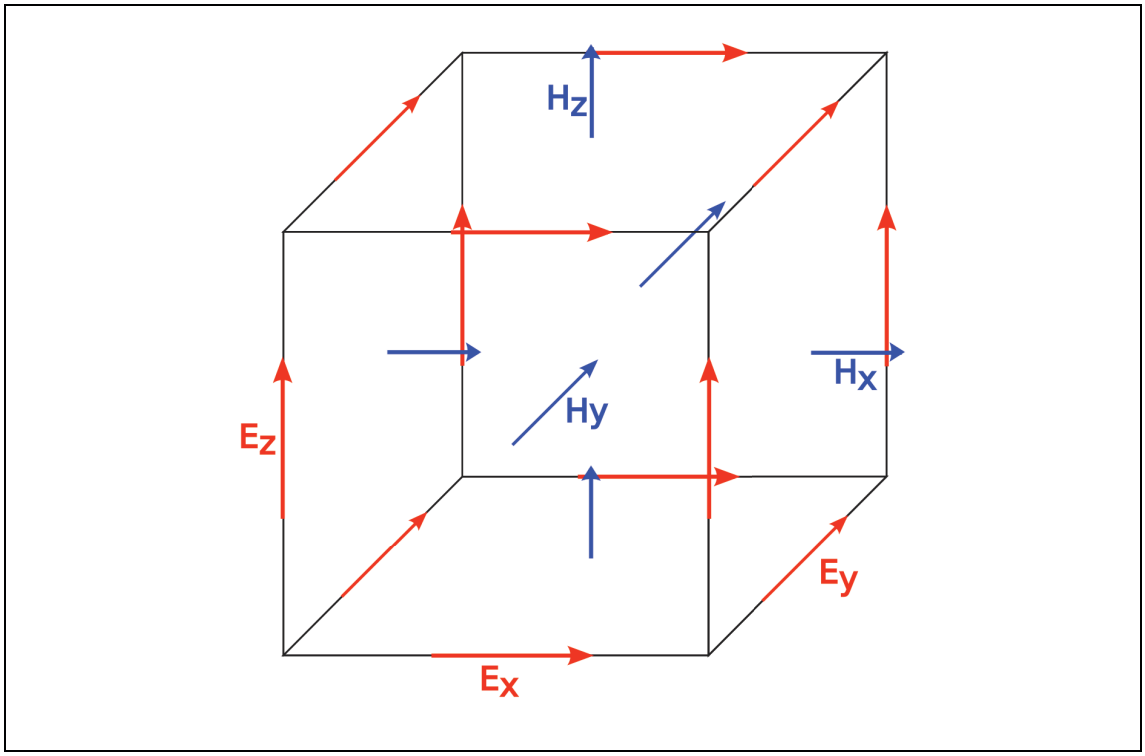

Figure 2-2: Representative Yee Cell used in FDTD simulations with Lumerical.

For simulations with radiation that propagate to infinity, it is necessary to truncate the domain such that the computation can be completed in a reasonable amount of time. In such instances, the boundary that surrounds the domain must act as if it allows radiation to pass through and not reflect radiation back in to the simulation region. Berenger developed such boundary, called Perfectly Matched Layers (PML) [17].

Finite-difference time-domain calculations are computationally time intensive, therefore simulation domains are limited to the objects of interests and the near-field scattering patterns. For our experiment, FDTD was performed for the metallic film and the nanoaperture, and the area immediately before and after the nanoaperture. To obtain the scattered light pattern in the far-field, a near-to-far-field transformation was performed.

2.2.2 Near-to-far-field Transformation

Far-field transformation was used to reduce computation time when the observation points or locations are sufficiently far away from the scattering object (an order of magnitude away compared to the dimension of the object). Simulation of the space between the observation location and the object would then be unnecessary.

The method of near-to-far-field transformation for FDTD was developed by Umashankar and Taflove [18]. The method consists of placing a virtual surface surrounding the scattering object of interest. The electric and magnetic fields for the surface are obtained using FDTD. By integrating the tangential fields on the virtual surface, the far-field radiation pattern can be calculated.

The benefit of this method is that instead of having to integrate the currents on the complex surface of the object of interests, the surface equivalence theorem allows the integration to be performed on any arbitrary surface that surrounds the

object [19]. As such, simple surfaces that conform to the existing FDTD mesh can be chosen to simplify the integration.

For the simulations of the light emanated from the nanoaperture, the near-to-far-field transformation was applied to a surface 117nm from the back plane of the metallic surface. The transformation gives the radiated intensity in terms of the scattered angle.

2.2.3 Validation of Lumerical FDTD Results

The previous sections described the theoretical basis for FDTD. For the implementation of FDTD in our simulations, we used the commercially available simulation package Lumerical FDTD. It is a software tool developed for simulating electromagnetic waves, particularly applicable for experiments involving the propagation, diffraction, and scattering of optical radiation. More information can be found at the company website, www.lumerical.com.

To ensure that simulation results from the software are suitable for our experiment, we tried to replicate the analytical results in Garcia et al. [10] in Lumerical FDTD. The physical parameters described in the paper were duplicated within Lumerical: corrugation periods = 500nm, aperture diameter and corrugation width = 40nm, corrugation depth = 83.5nm, and illumination wavelength 532nm. Figure 2-3 compares the results from Lumerical and Garcia et al. [10] for the intensity distribution of light as a function of distance from the

nanoaperture. It can be seen that they are nearly identical. As such, we were confident to proceed with the FDTD simulations using Lumerical.

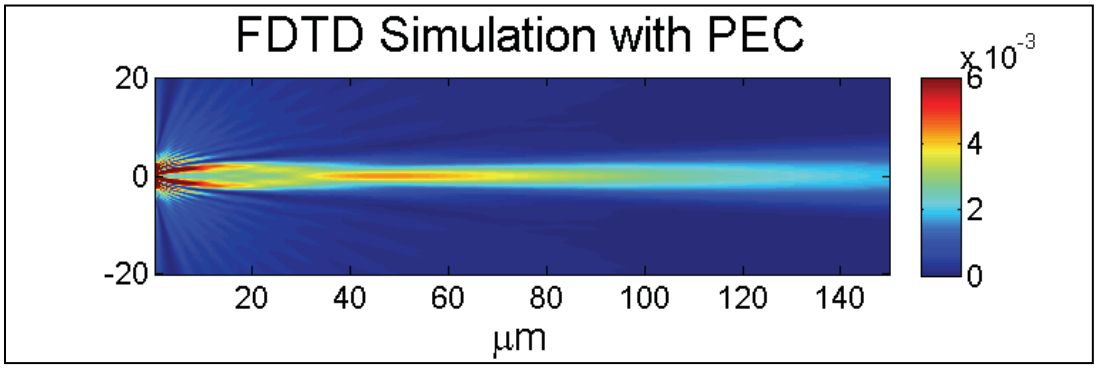

Figure 2-3: 2D intensity profile from FDTD simulation of nanoaperture with identical parameters to [10]

2.3 Summary

In this chapter the theory behind the formation of surface plasmons and the application to beaming light through a nanoaperture surrounded by periodic corrugations was introduced. Two models for the recoupling of light from the corrugations were presented: the perfect conductor model and the quasi-perfect conductor model. In the latter half of the chapter the mathematical theory for finite-difference time-domain was discussed. These tools will be used in Chapter 3 to investigate the different geometric parameters of the corrugations in perfect electrical conductors and real metals.

3 TWO-DIMENSIONAL SIMULATIONS OF SENSITIVITY ANALYSIS

Computational models of light emanating from a nanoaperture with periodic corrugations were performed using two methods: Finite-Difference Time-Domain (FDTD) and analytic computation based on Quasi-Perfect Conductor Model (QPCM). In this chapter, FDTD is used to explore the effects of the geometric parameters for beaming light through a nanoaperture. The parameters of the periodic corrugations investigated are the number of rings, corrugation depth, corrugation width, and corrugation period. A discussion of the effects of the parameters is presented at the end of this chapter.

3.1 Finite-Difference Time-Domain Simulations

Lumerical FDTD was used to simulate the different parameters that would give the optimal beaming effect for 532nm wavelength. Lumerical is a commercial software package designed to simulate the propagation of electromagnetic waves in 2D or 3D. To reduce computation time, simulations were performed on the Glacier cluster of Westgrid, the Western Canada Research Grid for high performance computing.

The geometry of the corrugated aperture is show in Figure 3-1. A is the corrugation width, P is the corrugation period, D is the aperture diameter, H is the corrugation depth, and N is the number of corrugations. The dependence of

beaming light from the nanoaperture based on these parameters is investigated through simulations below. The title of each 2D result obtained from Lumerical contains the material examined, and the values of the corrugation parameters used in the simulation.

A model of the aperture cross-section was created in the CAD interface of Lumerical. A plane wave source propagating along the x-axis, with the electric field parallel to the y-axis and perpendicular to the corrugations, illuminated the aperture. The source was monochromatic and centered at 532nm (green). A symmetrical boundary was placed along the center axis so that only half of the structure needed to be simulated. Monitors (the locations where the program was recording the wavefronts during simulation) were set to record 532nm wavelengths only, as required by the Lumerical FDTD software.

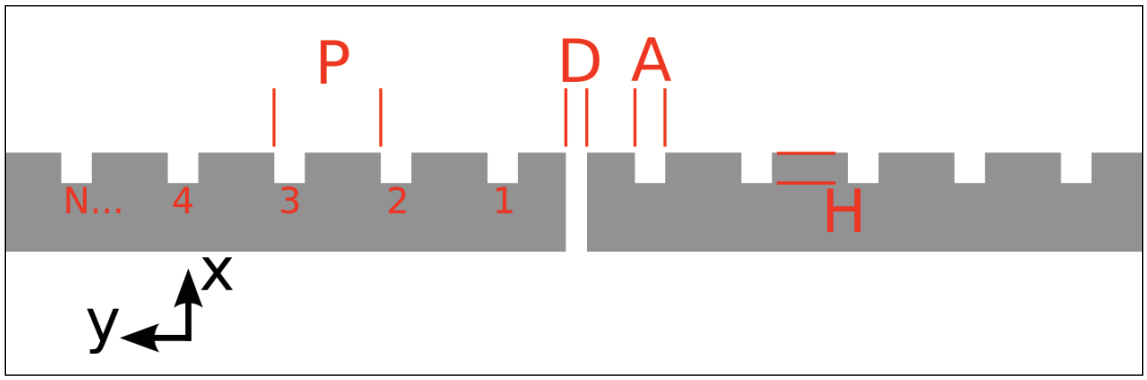

Figure 3-1: Profile view of bull's eye aperture showing the relevant geometric parameters.

Different parameters of the geometry were varied to find the optimal specification for beaming. To investigate how each parameter affected beaming, each parameter was iterated through a set of values while the other parameters were

held constant. The default values for the parameters, based on the design by Garcia et al. [10], are as follows: number of corrugations – 10; corrugation depth – 60nm; corrugation period – 500nm; corrugation width – 40nm; aperture width – 40nm. The PEC was simulated to confirm that we were in the right location to get beaming, and the effects of changing the parameters were investigated through simulation. The simulations were also performed for the Ag and Au to investigate the effects of surface plasmon assisted beaming through nanoapertures for real metals.

3.1.1 Number of Corrugations

The intensity pattern from a nanoaperture without surrounding corrugations is broadly distributed amongst all angles due to strong diffraction, as shown in Figure 3-2. Simulations for PEC were performed where the number of corrugations surrounding the nanoaperture was varied from one to ten and the results are presented in Figure 3-3. The resulting intensity patterns are different than the pattern from “zero” corrugations seen in Figure 3-2.

As corrugations are added to the FDTD simulation for PEC, the angular transmission maxima and minima begin to form. Beyond four corrugations, a dominant beam forms at 0°. In Figure 3-4, a line intensity profile is extracted from each simulation along the optical axis allowing the location of a local maximum to be observed. The beam width is also plotted at the location of the maximum in Figure 3-4. As the number of corrugations increases, the location of the maximum moves away from the aperture.

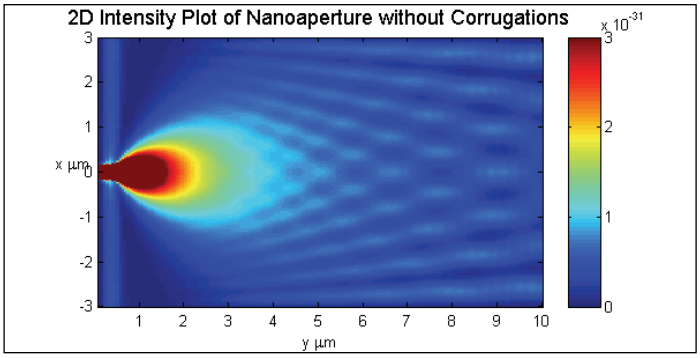

Figure 3-2: Intensity profile from a nanoaperture without surrounding corrugations.

The corresponding 2D simulations and line profiles for gold and silver films are presented in Figure 3-5 and Figure 3-7. In the sequence of simulations for the number of corrugations, a maximum does form beyond the location of the aperture at the metal film. Also, as can be observed from the cross section of the intensity pattern in Figure 3-6 and Figure 3-8, the highest intensity does not occur at the central axis, but instead is observed at a distribution of angles.

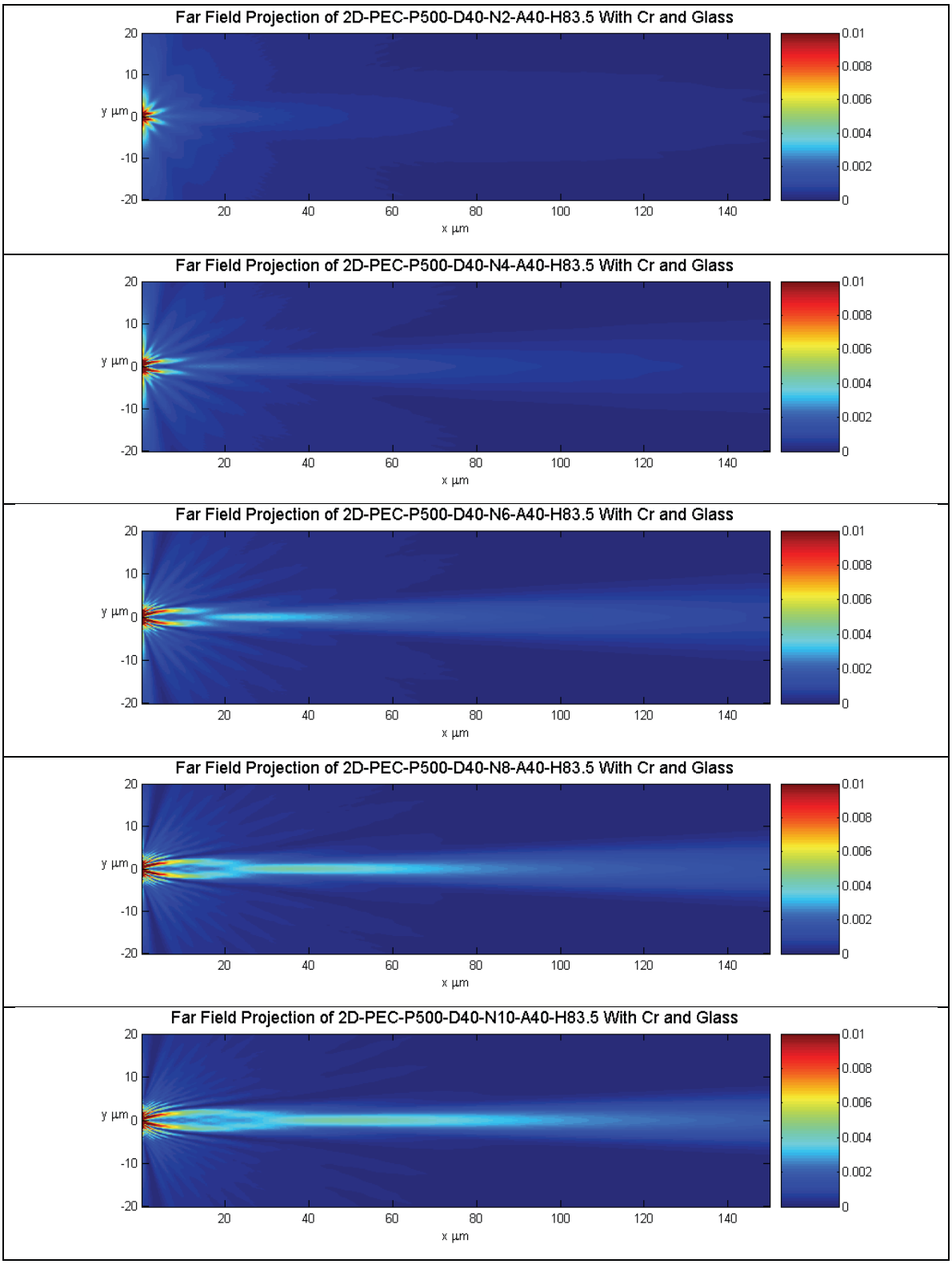

Figure 3-3: 2D intensity profile of nanoapertures in PEC with varying numbers of corrugations. N* in the figure titles show the number of corrugations.

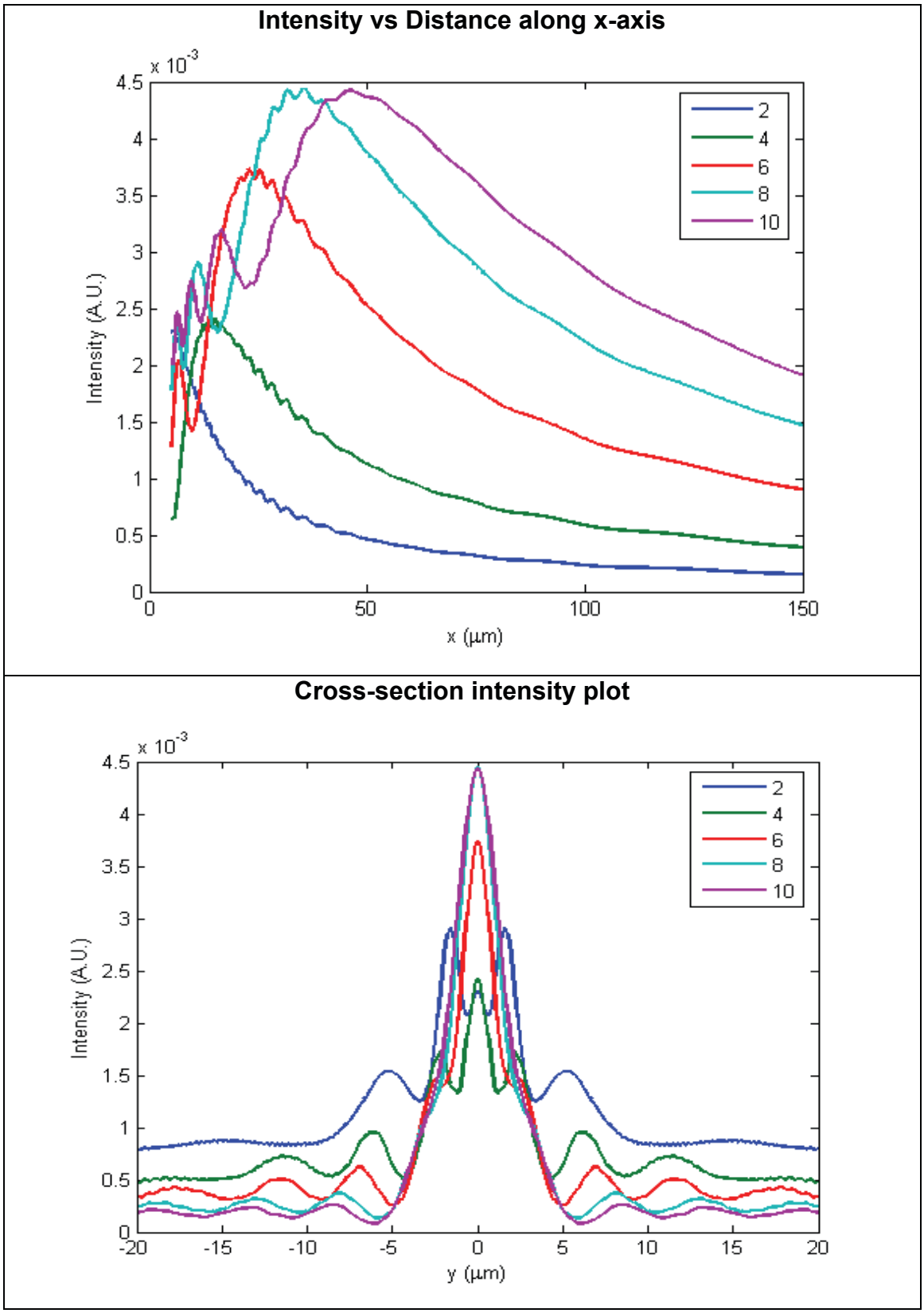

Figure 3-4: Top) Intensity plot for PEC along x-axis, and Bottom) corresponding cross-section intensity plot at the maxima for increasing number of rings.

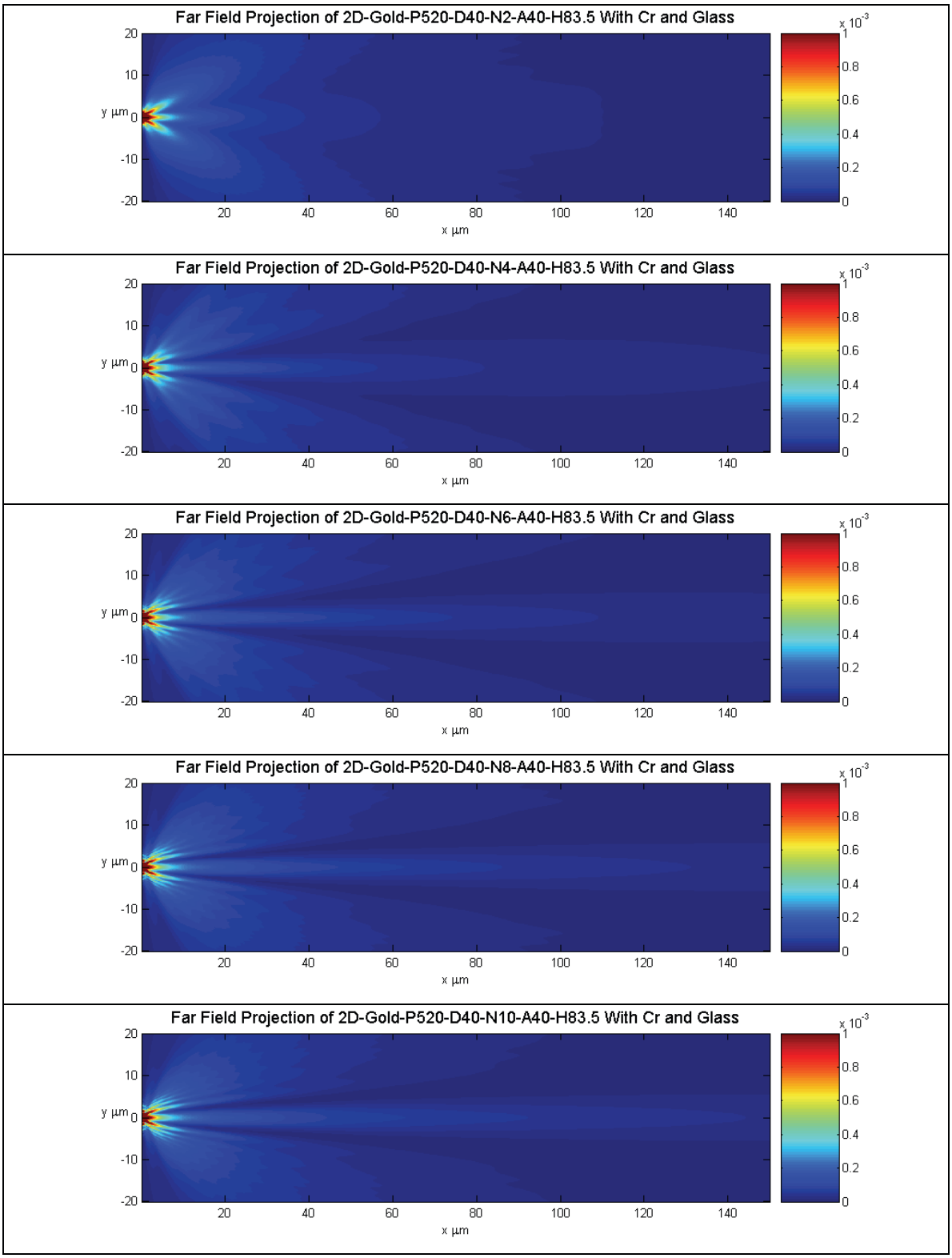

Figure 3-5: 2D intensity profile of nanoapertures in Gold with varying numbers of corrugations. N* in the figure titles show the number of corrugations.

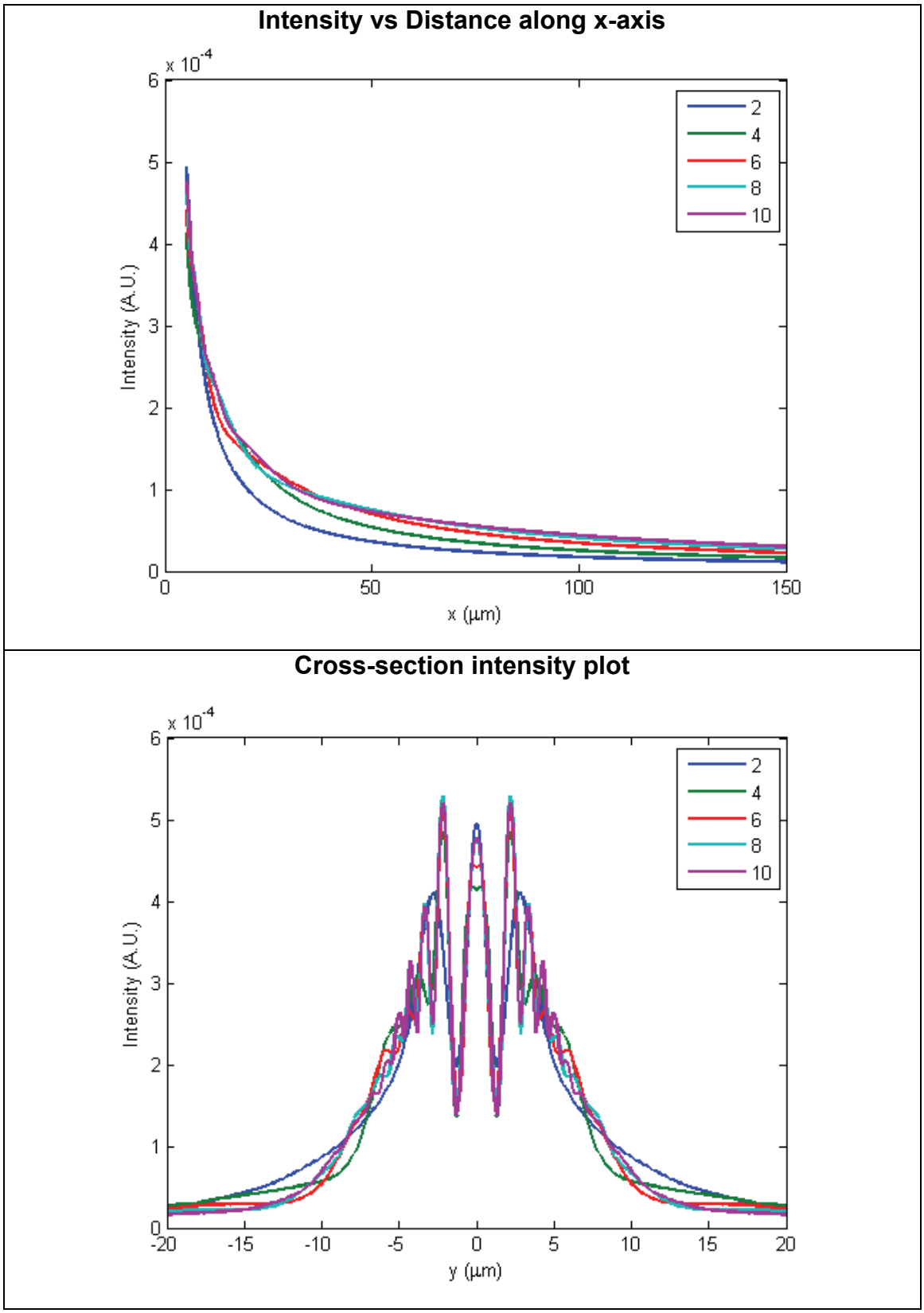

Figure 3-6: Top) Intensity plot for Gold along x-axis, and Bottom) corresponding cross-section intensity plot at the maxima for increasing number of rings.

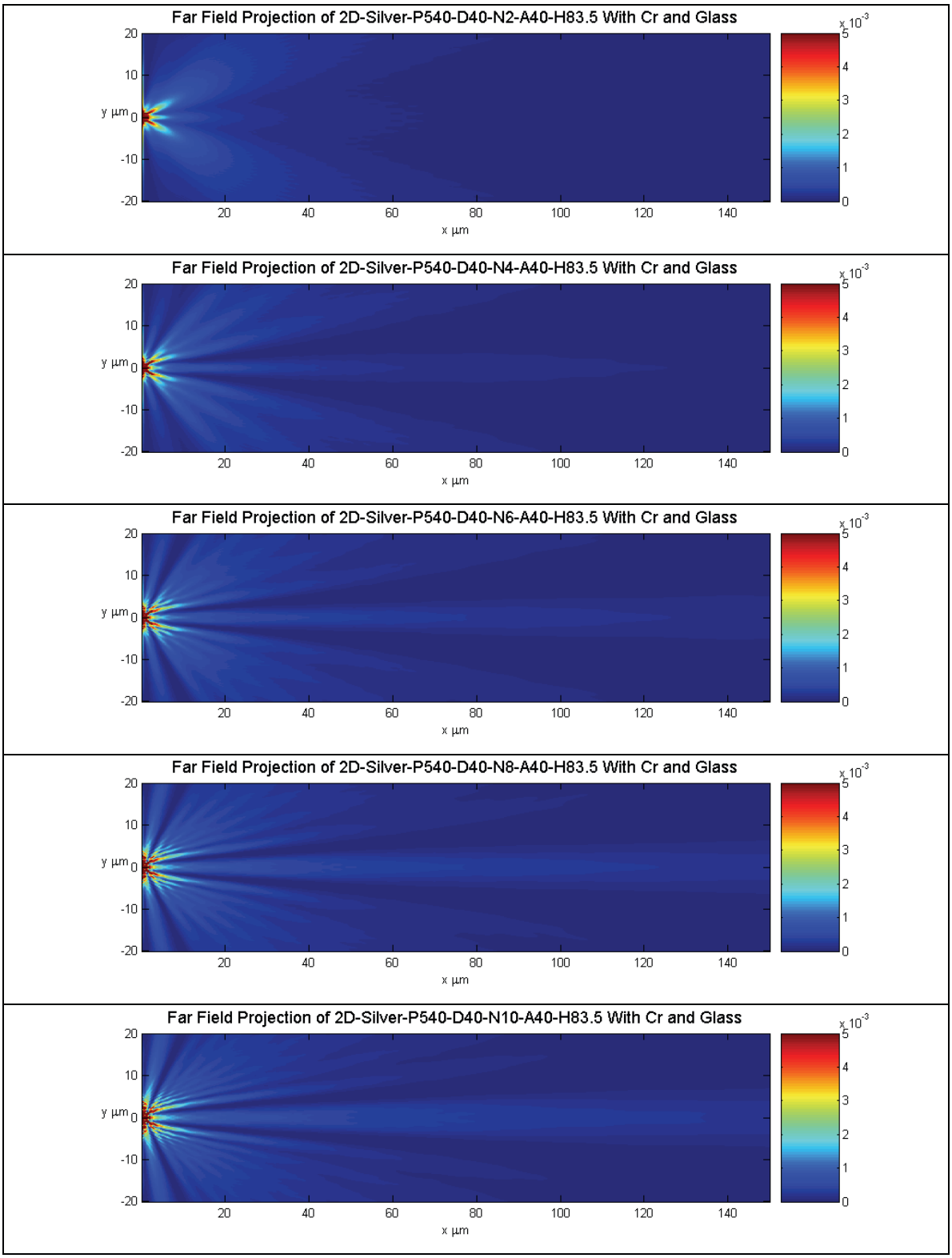

Figure 3-7: 2D intensity profile of nanoapertures in Silver with varying numbers of corrugations. N* in the figure titles show the number of corrugations.

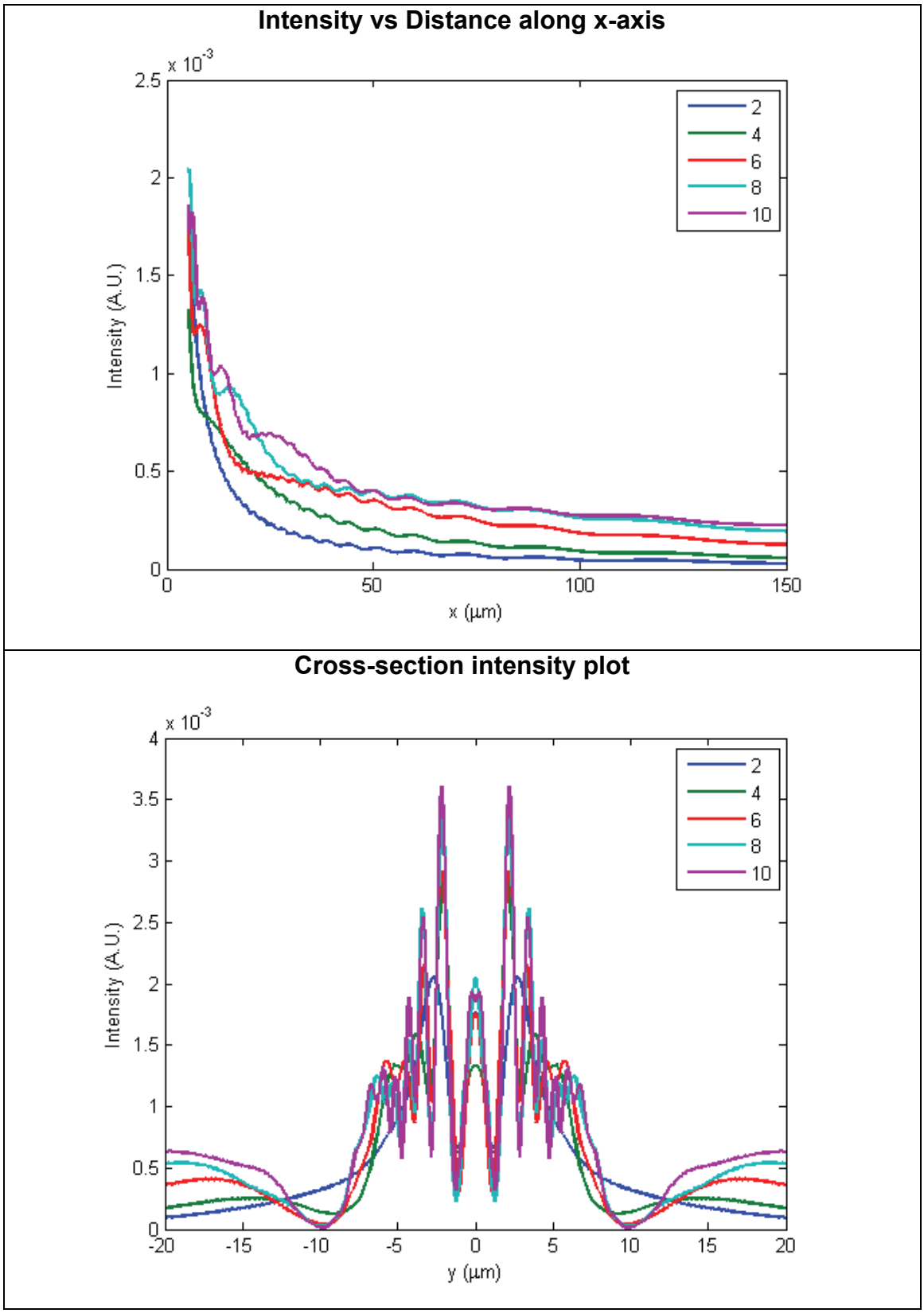

Figure 3-8: Top) Intensity plot for Silver along x-axis, and Bottom) corresponding cross-section intensity plot at the maxima for increasing number of rings.

3.1.2 Corrugation Period

Simulations were performed to investigate the effects of the corrugation period on beaming. For beaming, the corrugation period needs to be close to the wavelength of the light [10]. This parameter was iterated from 450nm to 560nm in 10nm increments, however only the results from 20nm steps are presented in Figure 3-9. In the PEC beaming can be observed for periods between 450nm to 500nm. The local maximum along the transmission axis moves away from the aperture as the period increases. Also, the secondary peaks from the interference pattern fan-in as the period increases. For the PEC, beaming occurs where the pattern converges in the middle. The line graphs of the axial and cross sectional intensity are presented in Figure 3-10.

The simulations investigating the effects of corrugation period in gold and silver films are presented in Figure 3-11 and Figure 3-13. Unlike with the PEC, the maximum intensity was located near the aperture at the film. For the gold films, although the simulation results did not predict a strong central beam, the cross sectional beam profile in Figure 3-12 indicated that power in the central beam was larger than the off axis components for corrugation periods between 520-540nm. For the silver films, the highest intensities always occurred off axis.

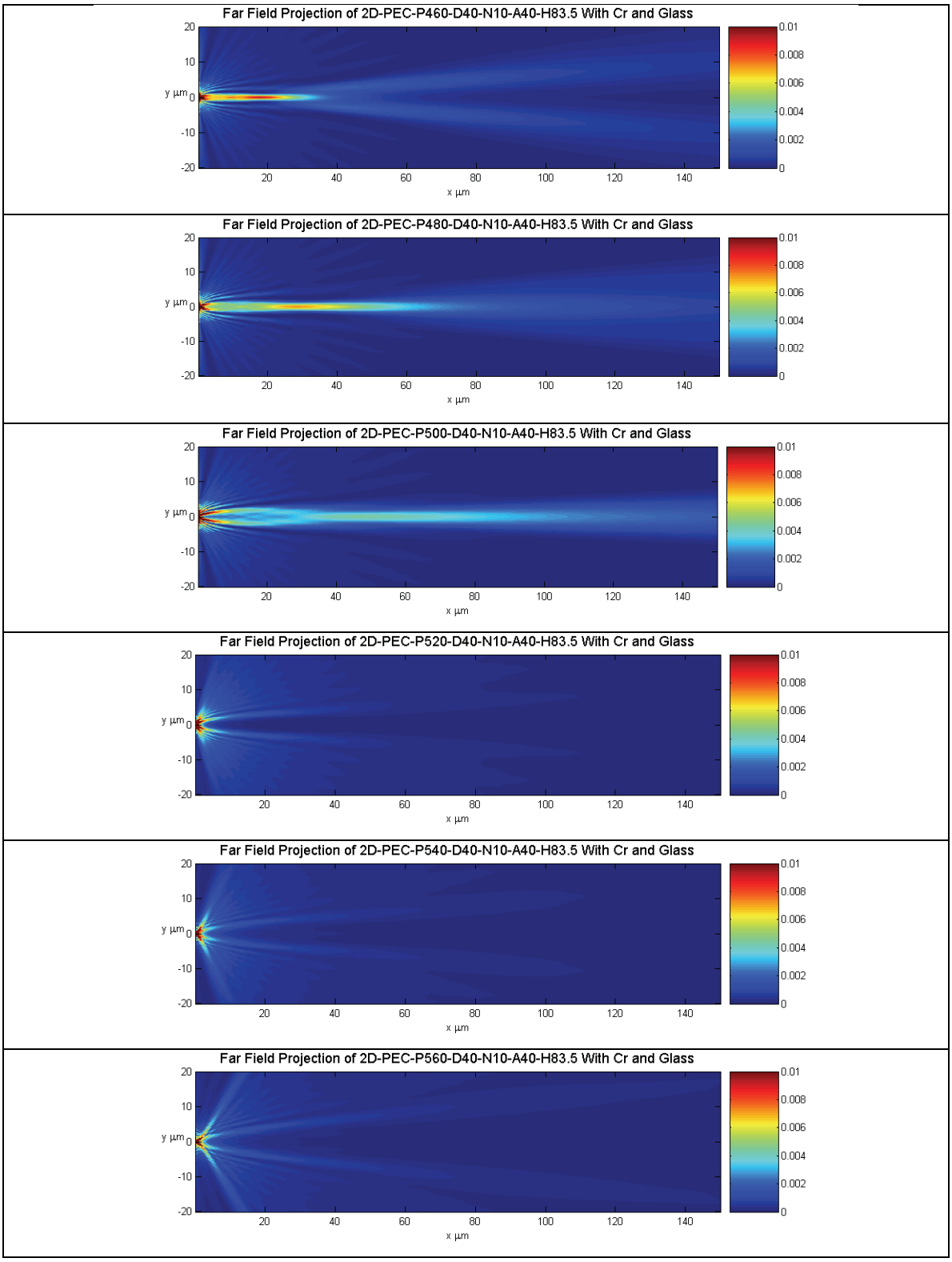

Figure 3-9: 2D intensity profile of nanoapertures in PEC with varying corrugation period. P* in the figure titles show the corrugation period.

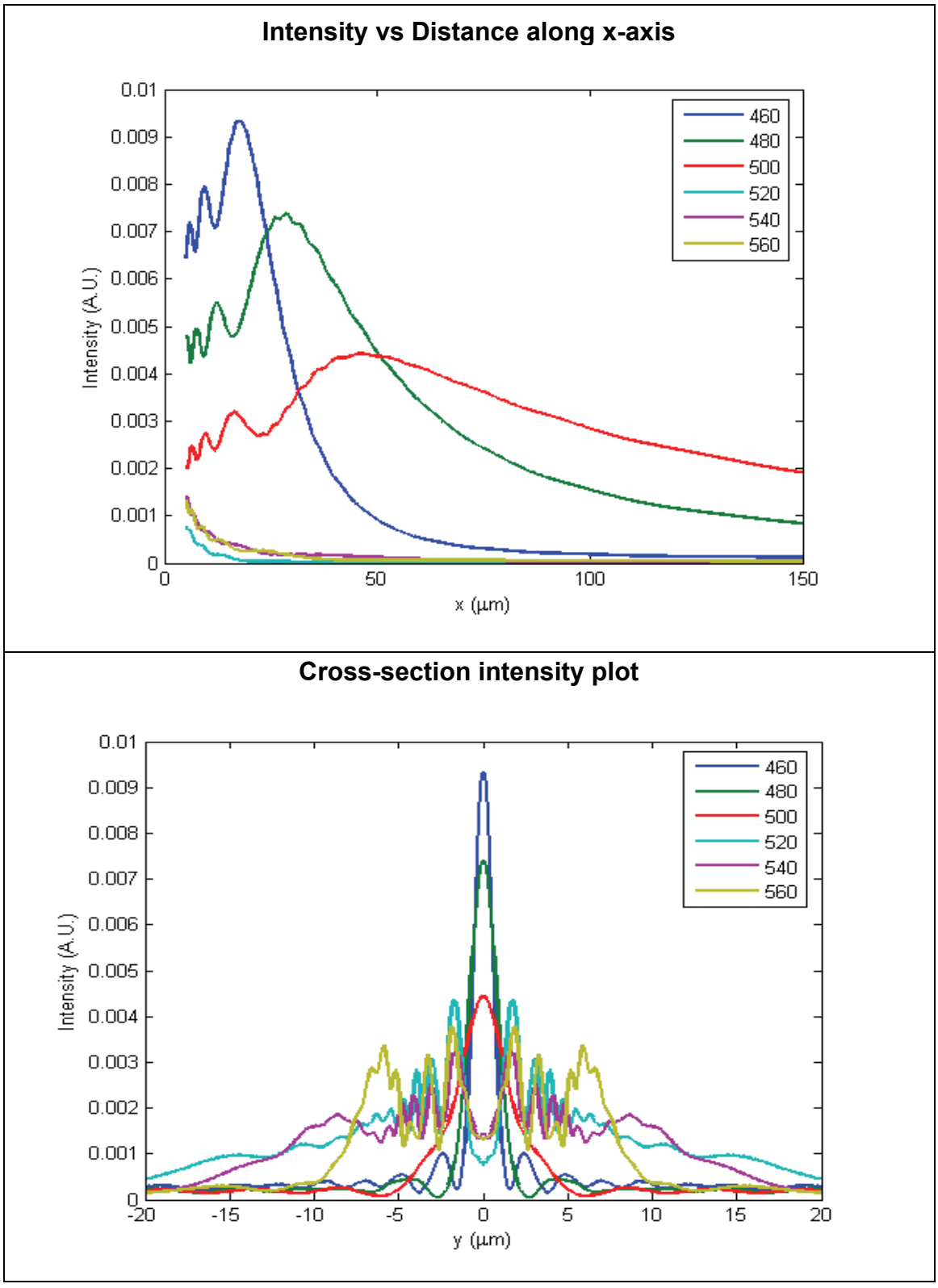

Figure 3-10: Top) Intensity plot for PEC along x-axis, and Bottom) corresponding cross-section intensity plot at the maxima.

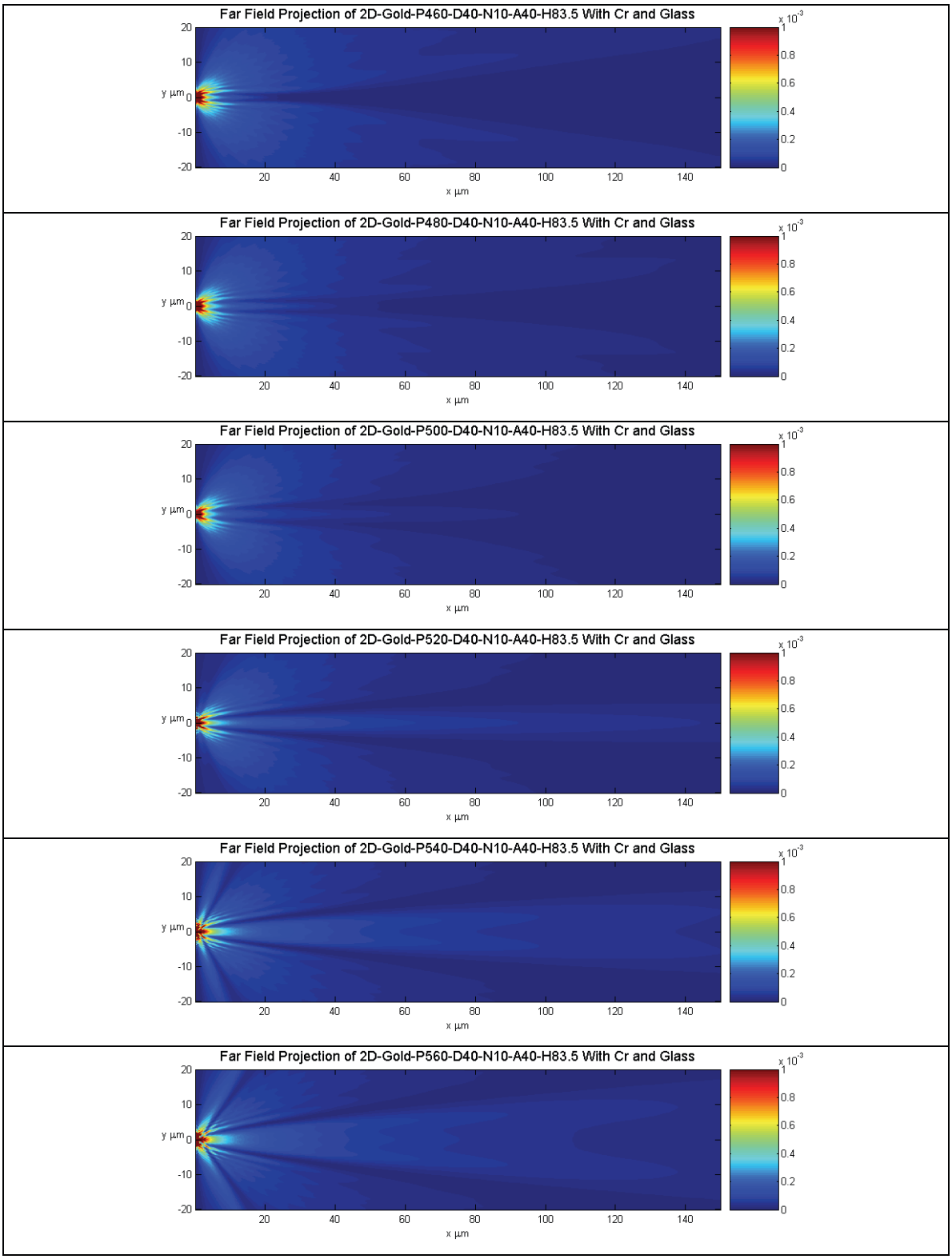

Figure 3-11: 2D intensity profile of nanoapertures in Gold with varying corrugation period. P* in the figure titles show the corrugation period.

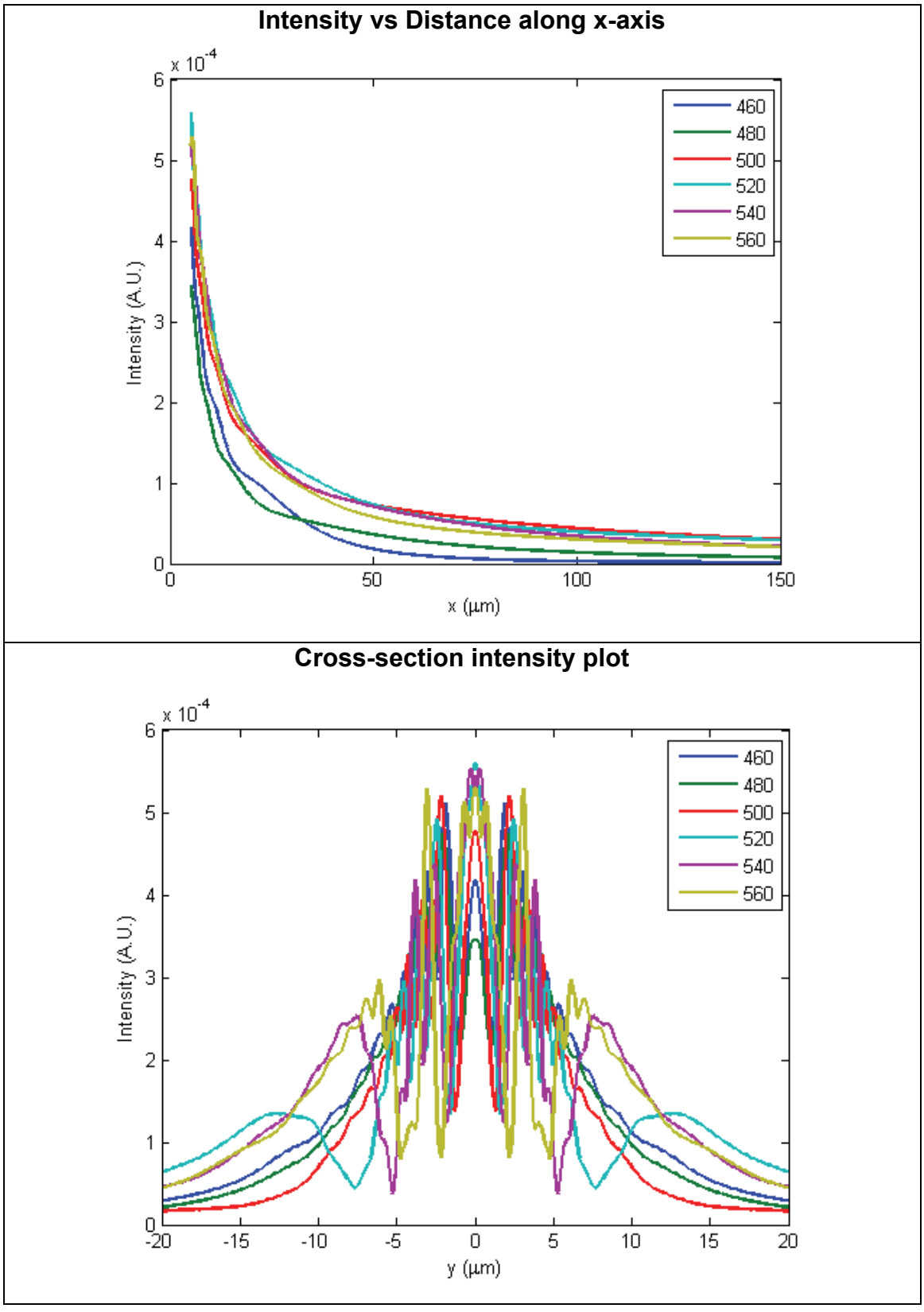

Figure 3-12: Top) Intensity plot for Gold along x-axis, and Bottom) corresponding cross-section intensity plot at the maxima.

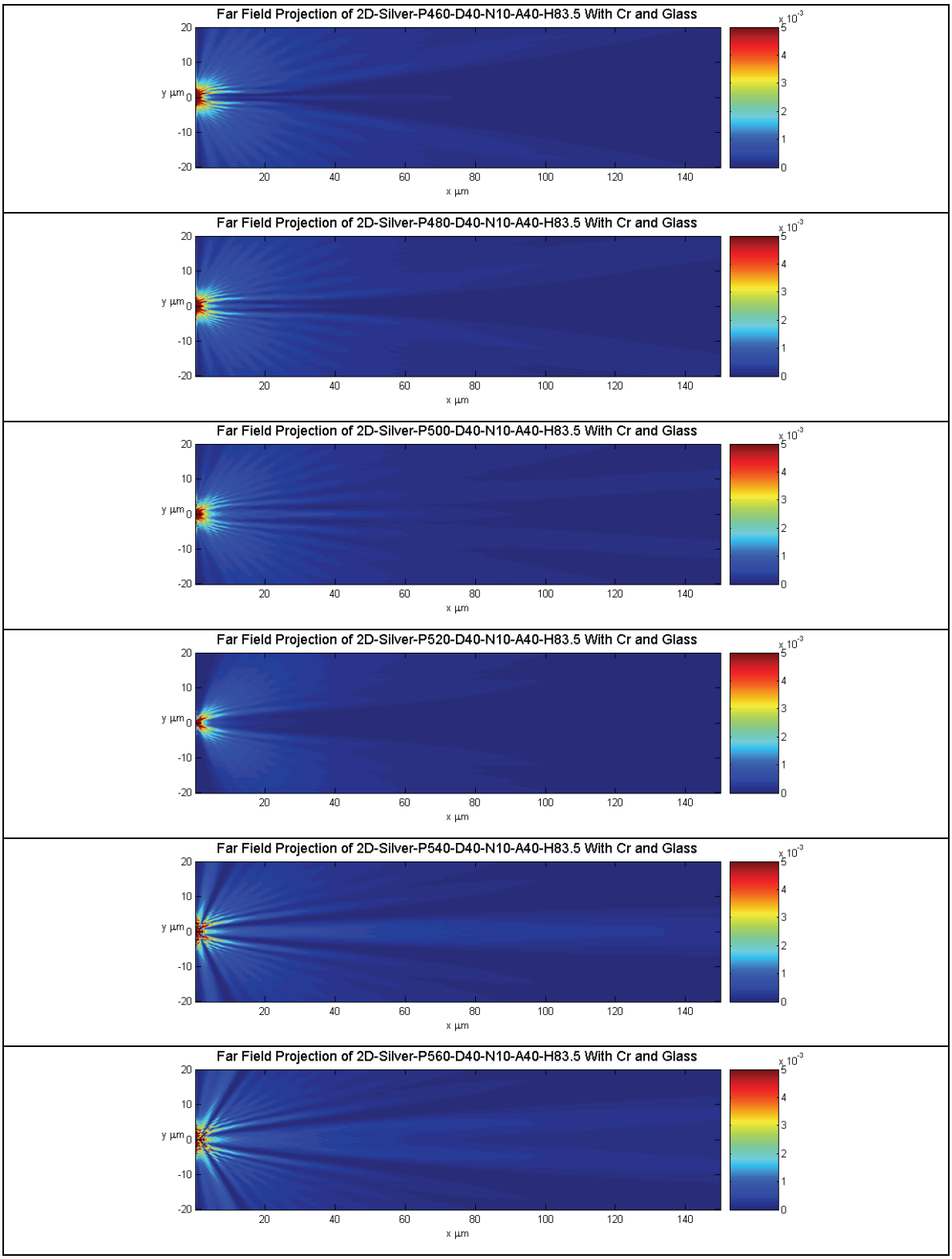

Figure 3-13: 2D intensity profile of nanoapertures in Silver with varying corrugation period. P* in the figure titles show the corrugation period.

Intensity vs Distance along x-axis

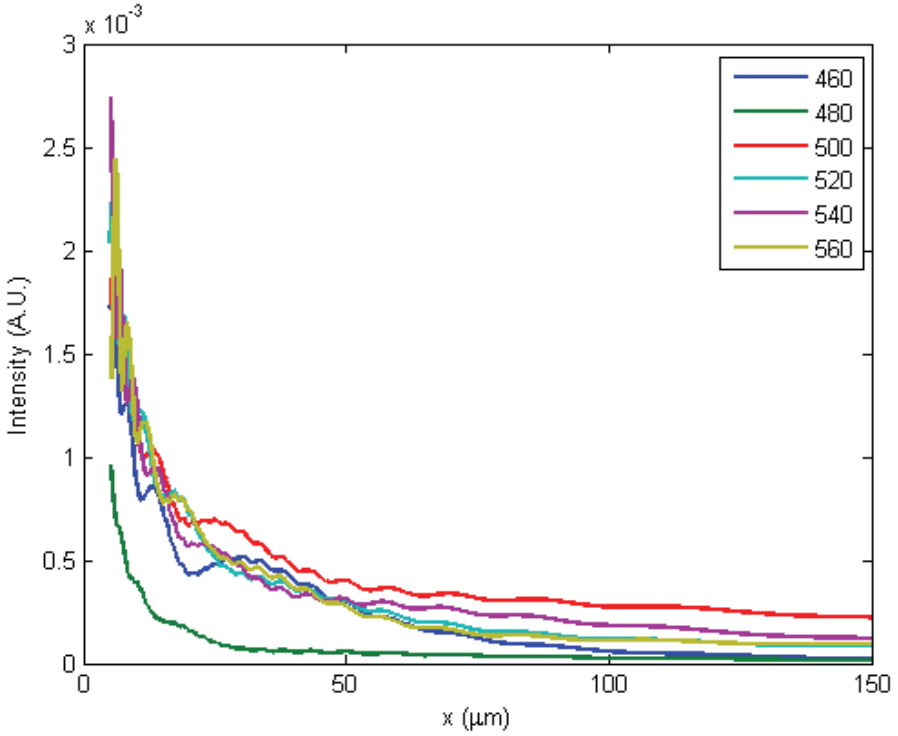

Cross-section intensity plot

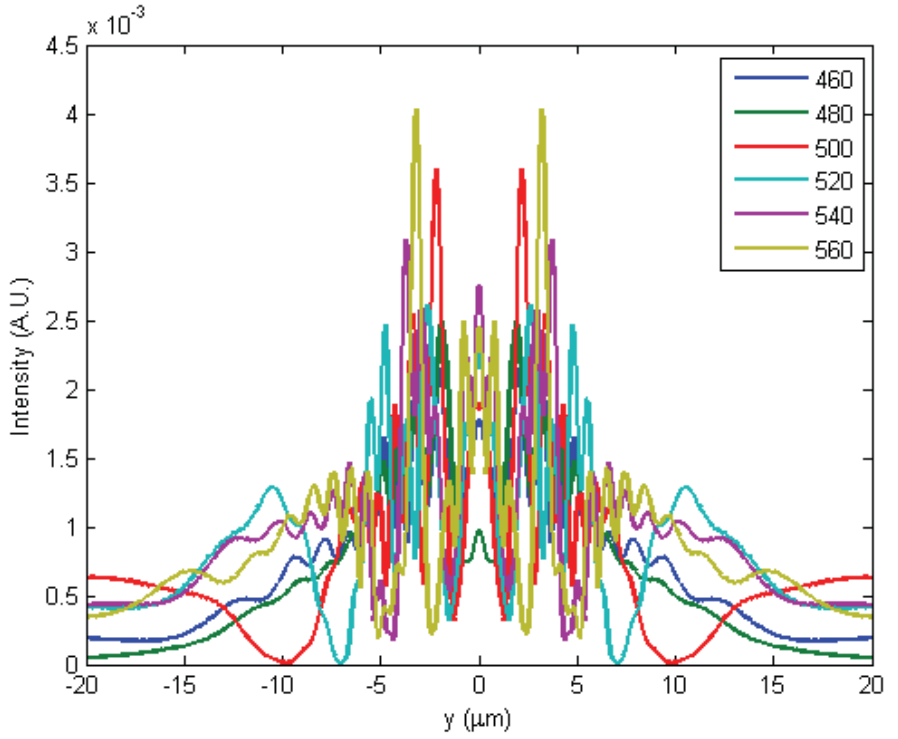

Figure 3-14: Top) Intensity plot for Silver along x-axis, and Bottom) corresponding cross-section intensity plot at the maxima.

3.1.3 Corrugation Depth

Simulations were performed to investigate the effects of the corrugation depth on beaming. Different corrugation depths, from 50nm to 120nm in 5nm increments, were simulated, but only the results in 10nm steps are presented in Figure 3-15. In the PEC, beaming is observed with increasing corrugation depth starting from 50nm, and a maximum beaming intensity was observed at 85nm. Beyond 90nm depth, the beam along the transmission axis vanishes. The line graphs of the axial and cross sectional intensity are presented in Figure 3-16.

The simulations investigation the effects of corrugation depth on beaming in gold and silver films are presented in Figure 3-17 and Figure 3-19 respectively. While both gold and silver films show some beaming along the transmission axis, significant secondary peaks are also present throughout the simulation domain for corrugation depth. The cross sectional beam profiles in Figure 3-18 and Figure 3-20 for gold and silver, respectively, shows the dominant secondary peaks.

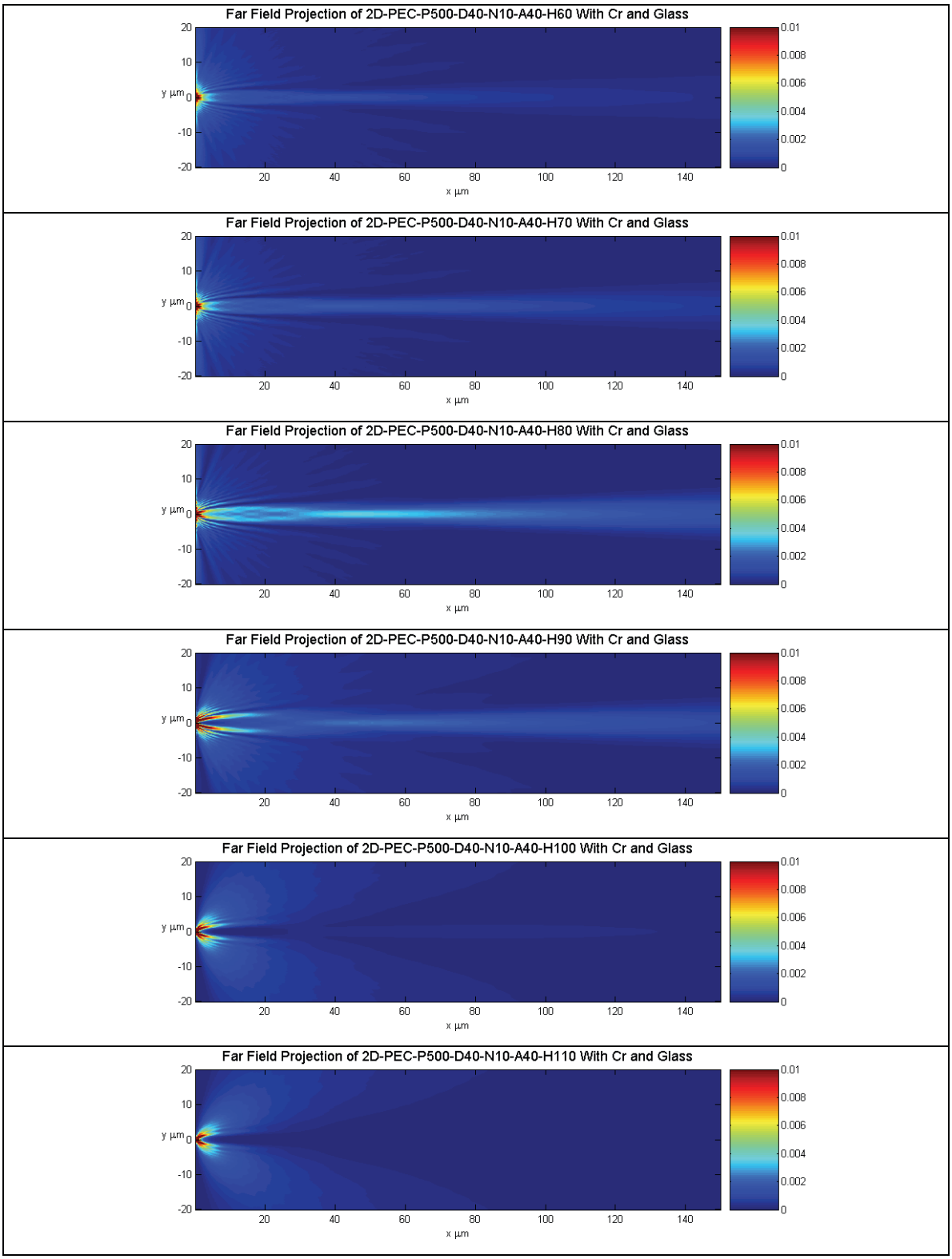

Figure 3-15: 2D intensity profile of nanoapertures in PEC with varying corrugation depth. H* in the figure titles show the corrugation depth.

Intensity vs Distance along x-axis

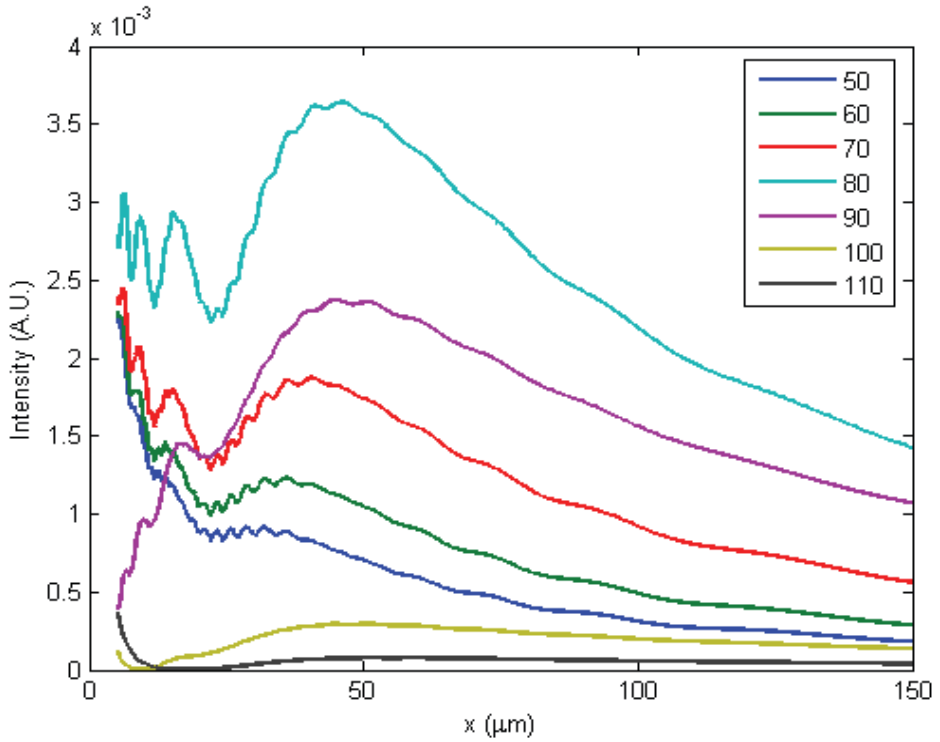

Cross-section intensity plot

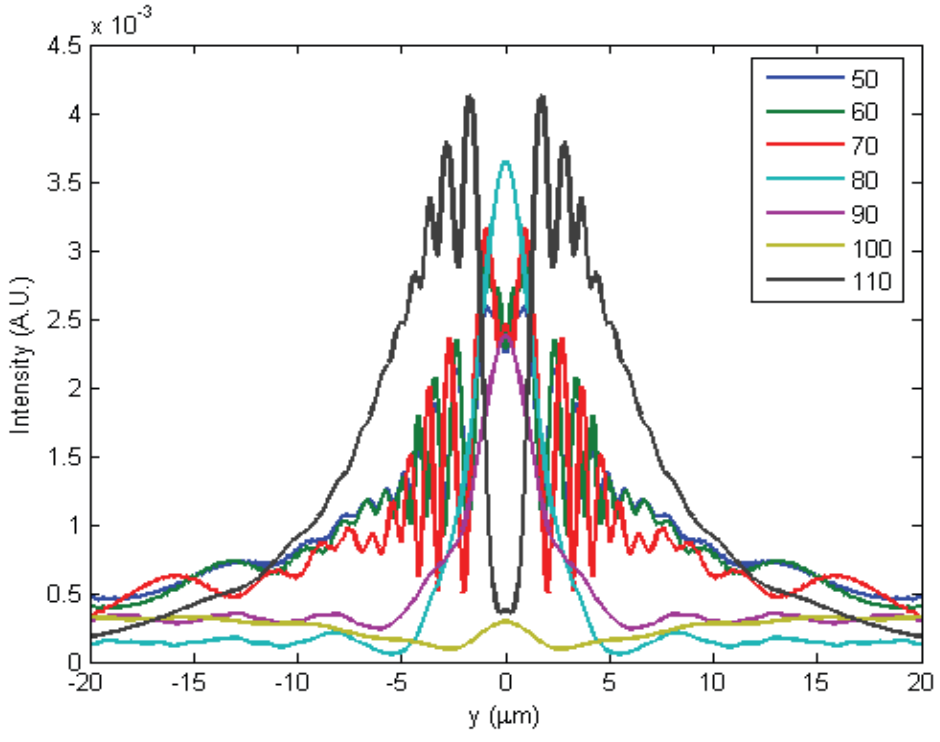

Figure 3-16: Top) Intensity plot of PEC along x-axis, and Bottom) corresponding cross-section intensity plot at the maxima.

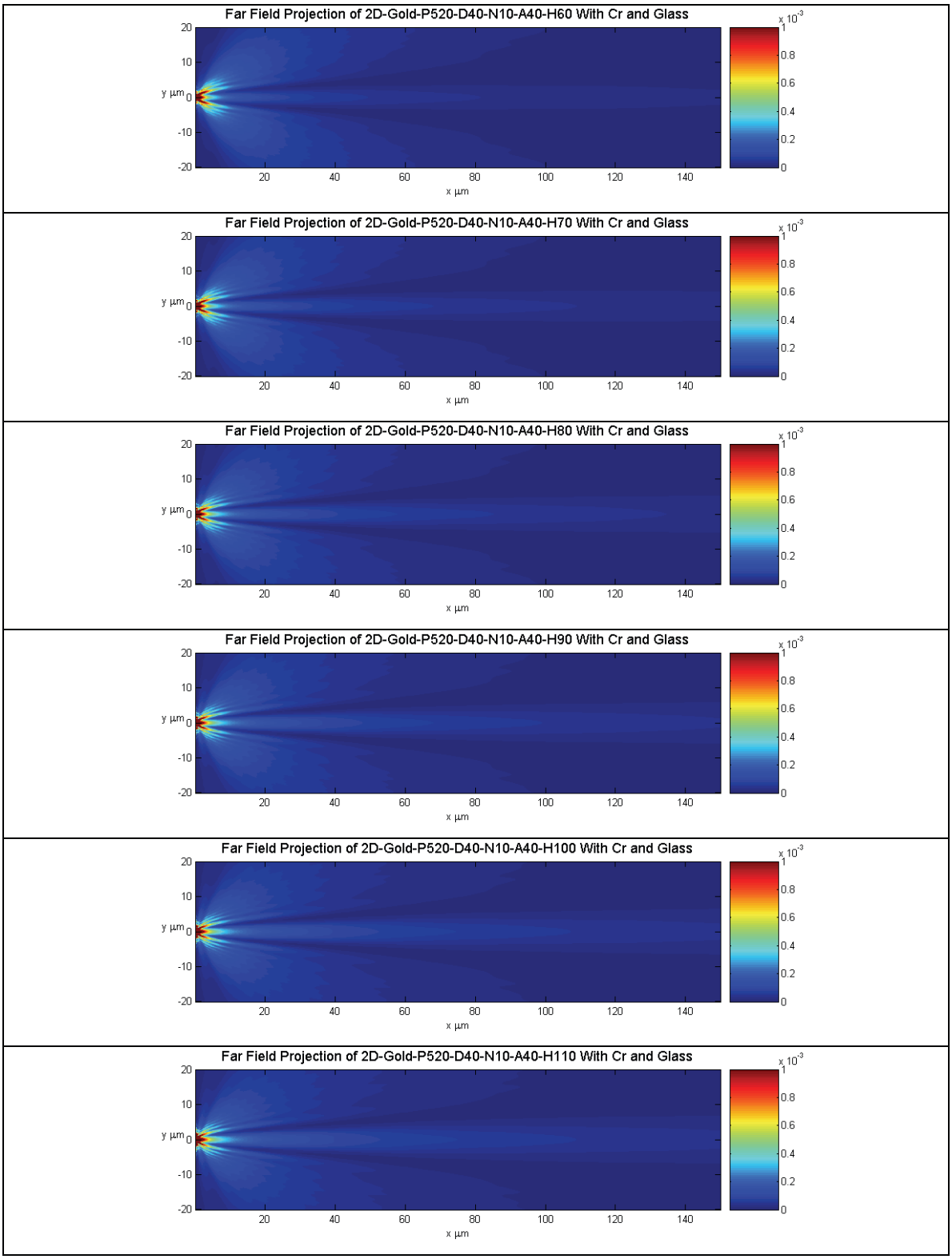

Figure 3-17: 2D intensity profile of nanoapertures in Gold with varying corrugation depth. H* in the figure titles show the corrugation depth.

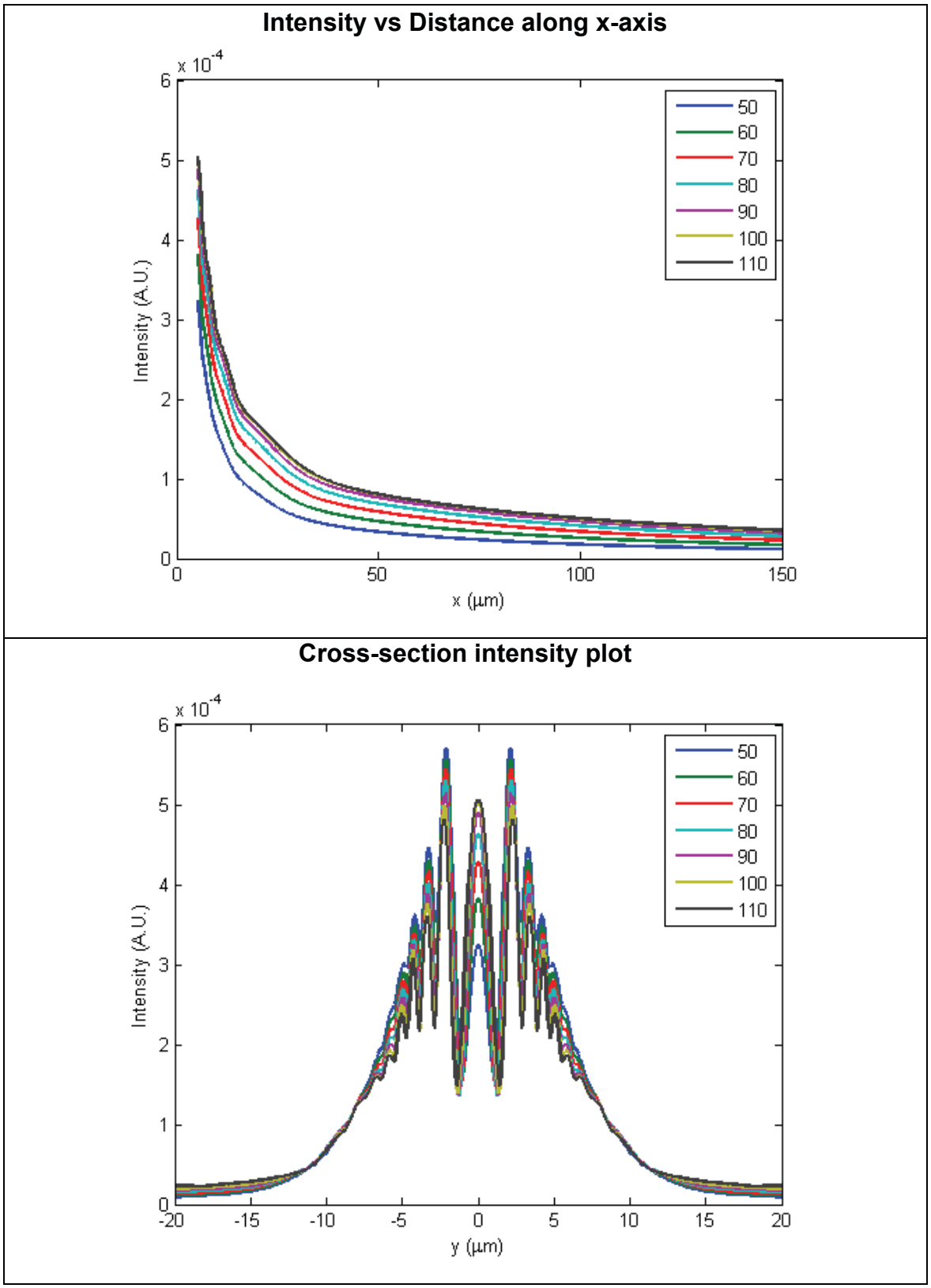

Figure 3-18: Top) Intensity plot of Gold along x-axis, and Bottom) corresponding cross-section intensity plot at the maxima.

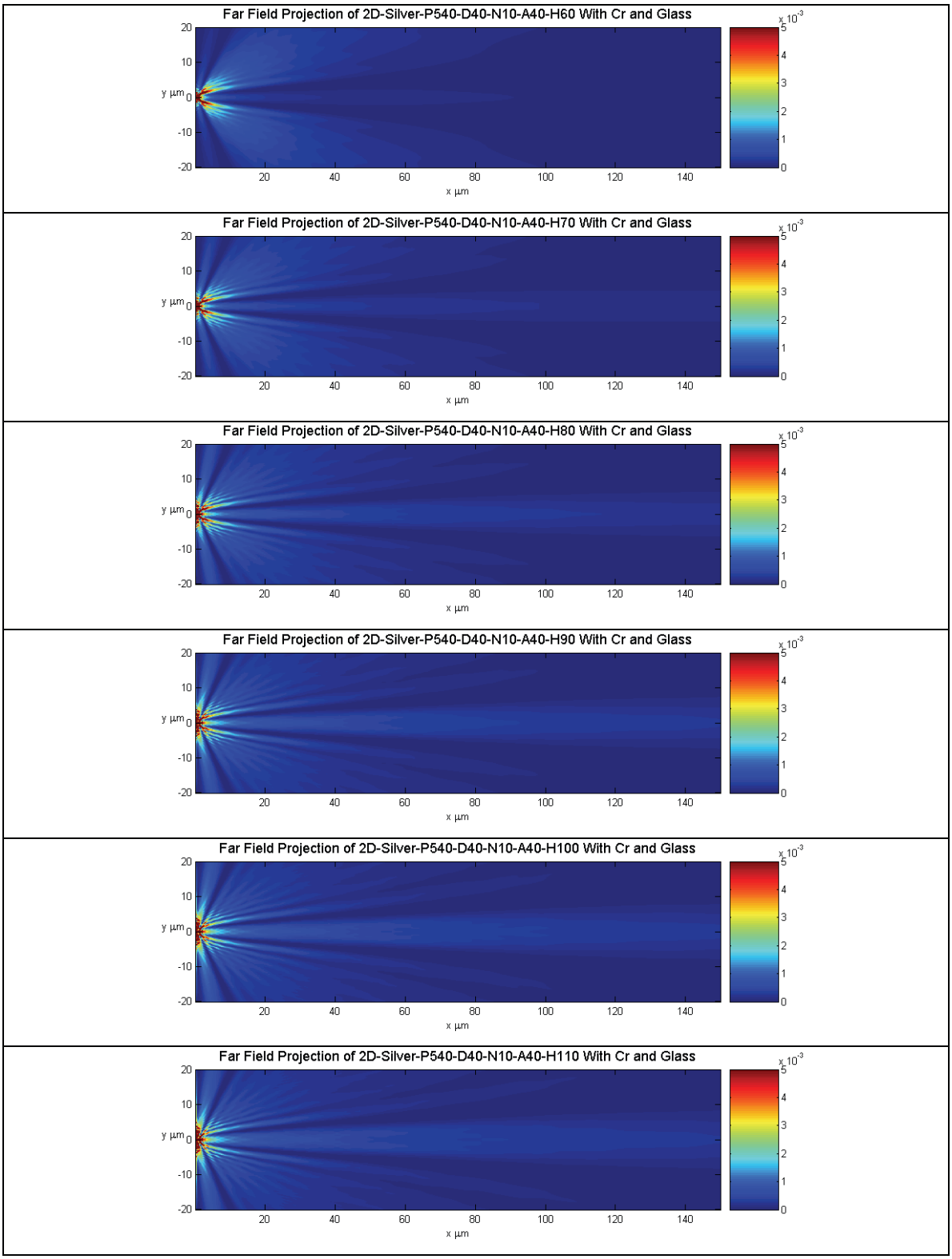

Figure 3-19: 2D intensity profile of nanoapertures in Silver with varying corrugation depth. H* in the figure titles show the corrugation depth.

Intensity vs Distance along x-axis

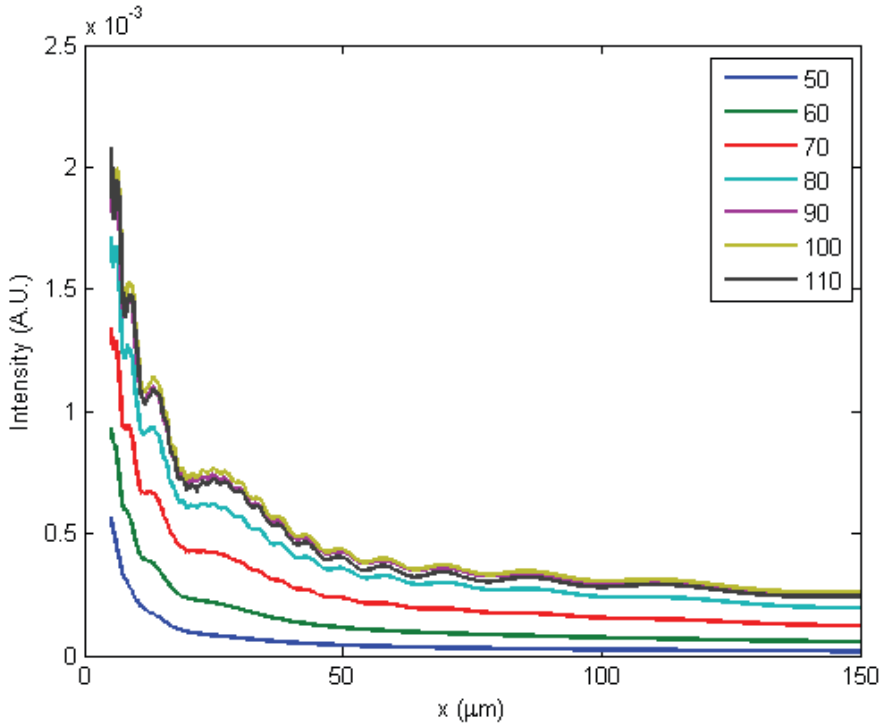

Cross-section intensity plot

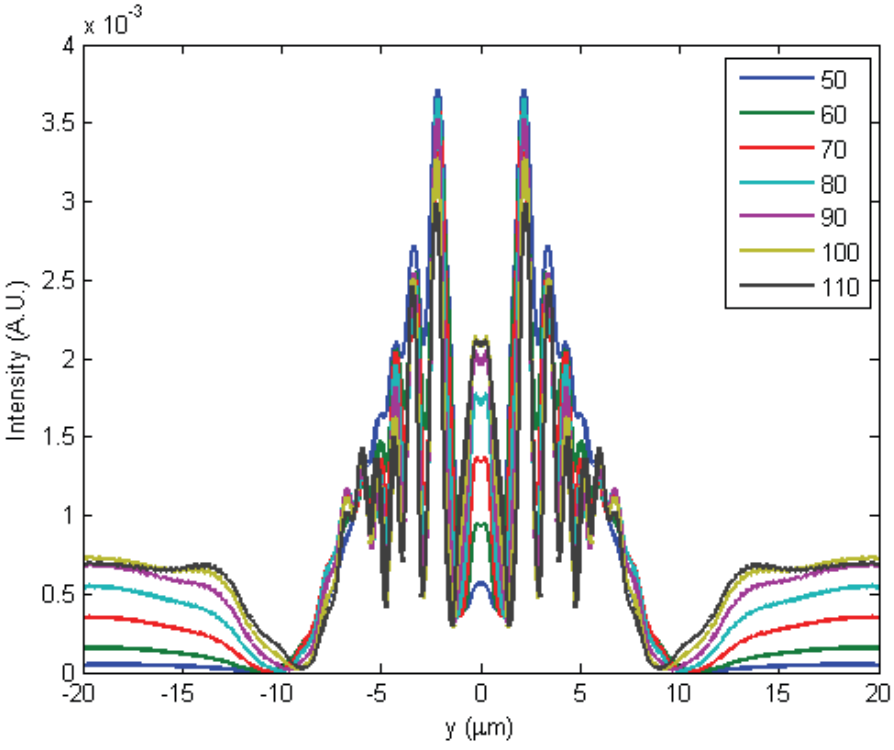

Figure 3-20: Top) Intensity plot of Silver along x-axis, and Bottom) corresponding cross-section intensity plot at the maxima.

3.1.4 Corrugation Width

Simulations were performed to investigate the effects of the corrugation widths, (given a fixed corrugation period), on beaming. The parameter was incremented from 40nm up to 250nm in 10nm steps, but only results for corrugation widths of 50nm, 100nm, 150nm, 200nm, and 250nm are presented in Figure 3-21. For the PEC, as the corrugation width increases, the local maximum along the transmission axis moves closer to the aperture. The line graphs of the axial and cross sectional intensity are presented in Figure 3-22.

The simulations investigating the effects of corrugation width in gold and silver films are presented in Figure 3-23 and Figure 3-25. For the gold films, a central beam along with strong off-axis beams can be observed for corrugation width of 50nm. As the width increased, the intensity of the central beam decreased until it vanished altogether beyond 150nm, leaving only the off-axis beams. Examination of the cross-section intensity plots for silver films suggests that even though some of the off-axis beams fan-in when corrugation width increased, the dominant peaks remain at a fixed angle.

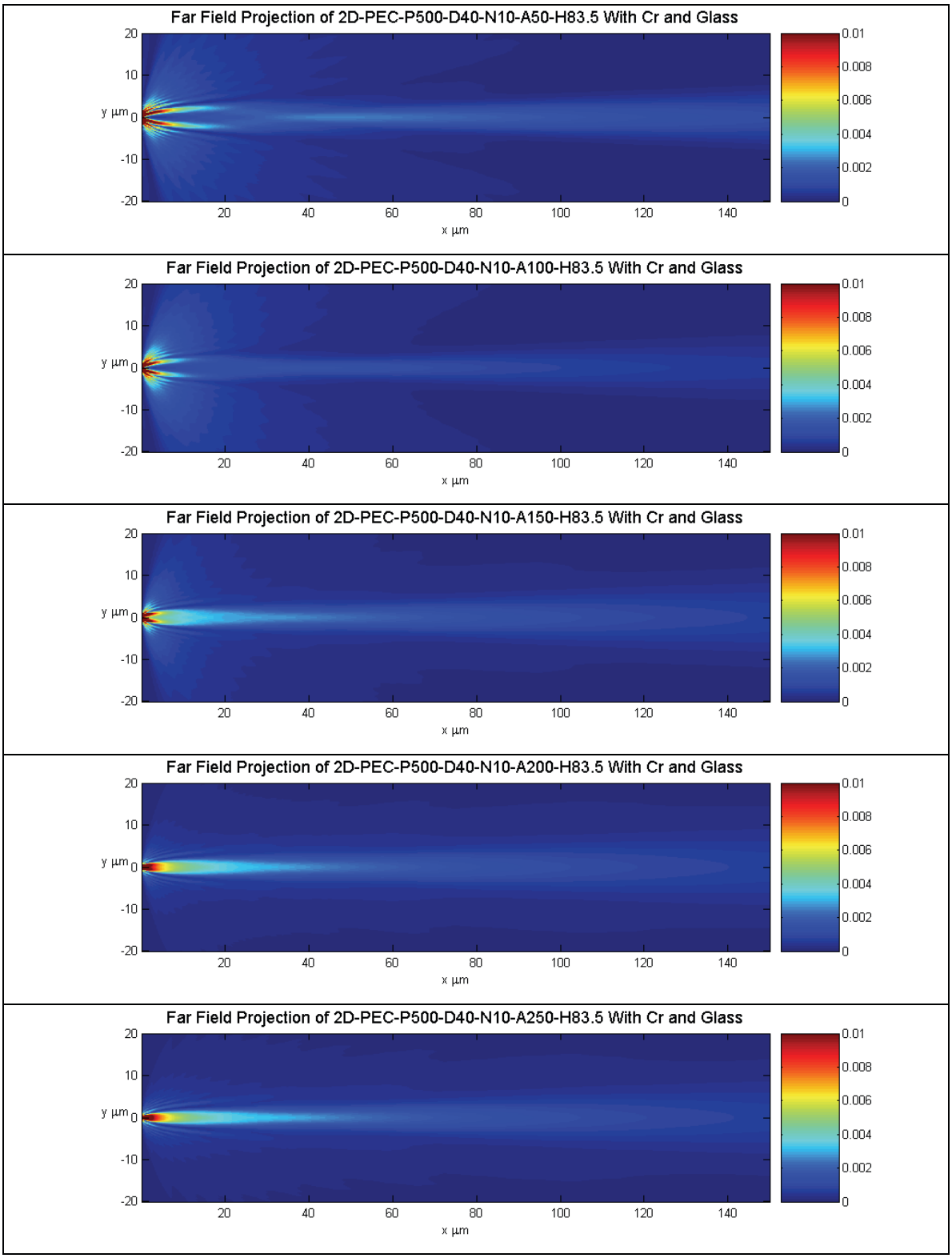

Figure 3-21: 2D intensity profile of nanoapertures in PEC with varying corrugation width. A* in the figure titles show the corrugation width.

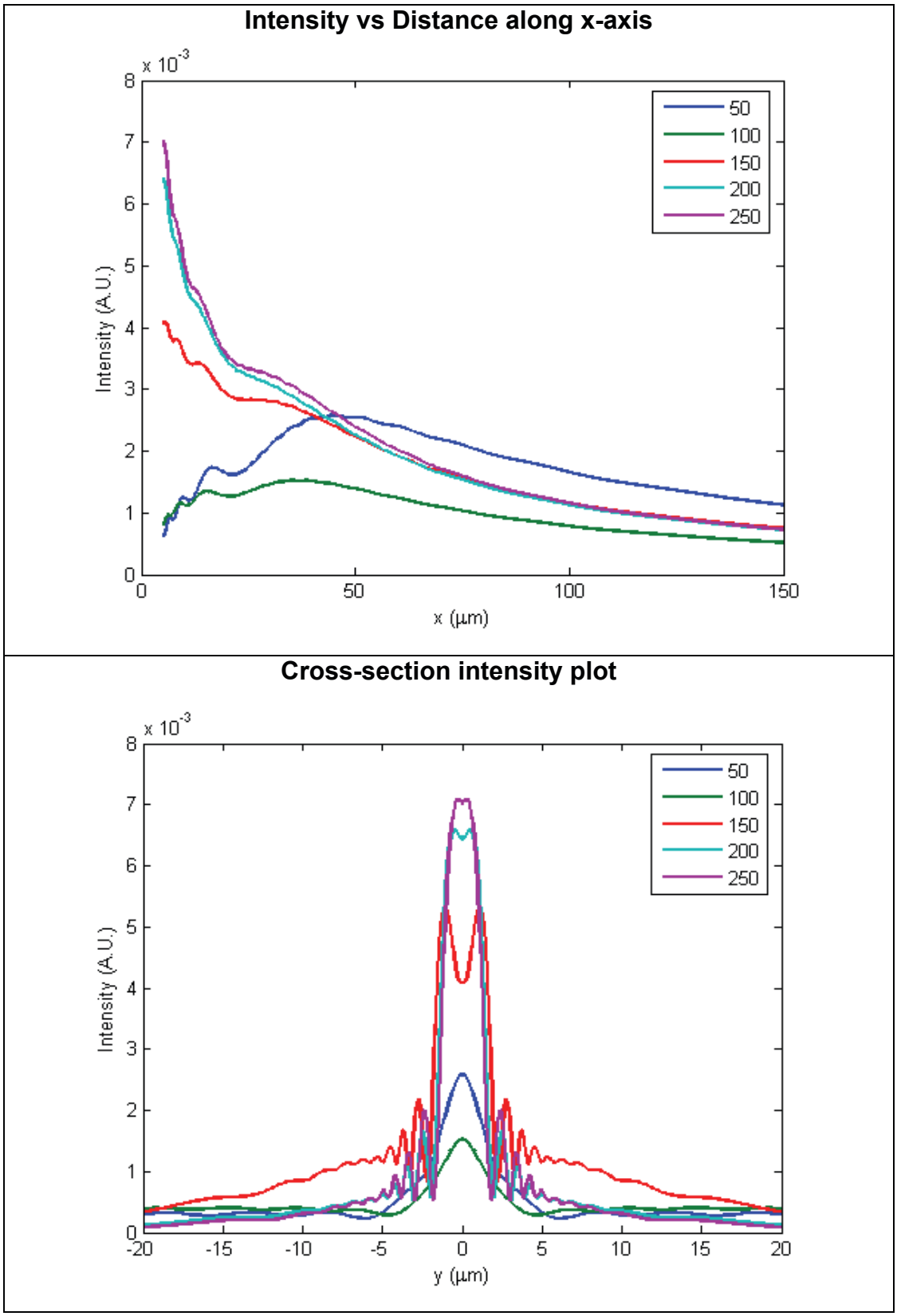

Figure 3-22: Top) Intensity plot of PEC along x-axis, and Bottom) corresponding cross-section intensity plot at the maxima of A.

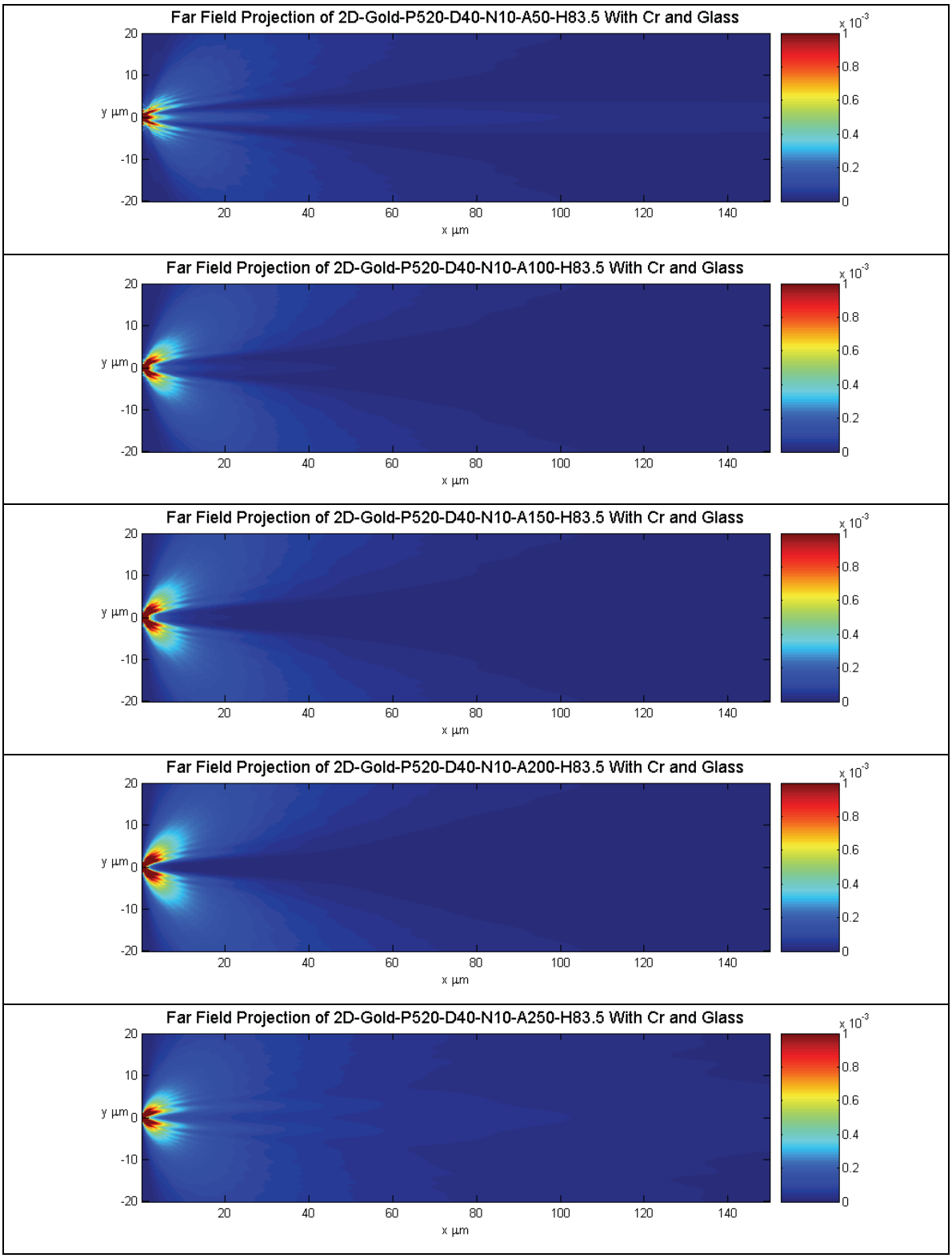

Figure 3-23: 2D intensity profile of nanoapertures in Gold with varying corrugation width. A* in the figure titles show the corrugation width.

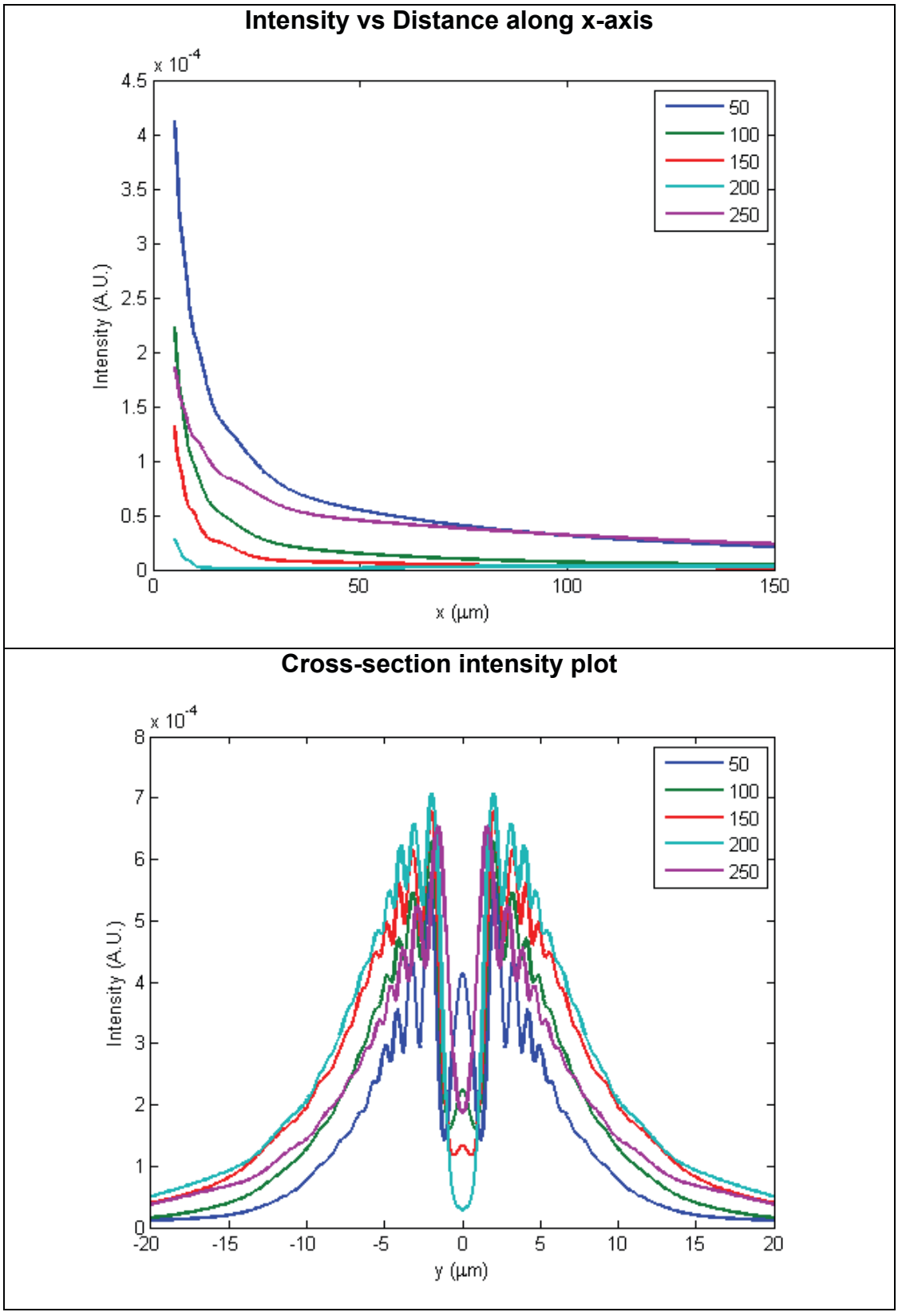

Figure 3-24: Top) Intensity plot of Gold along x-axis, and Bottom) corresponding cross-section intensity plot at the maxima of A.

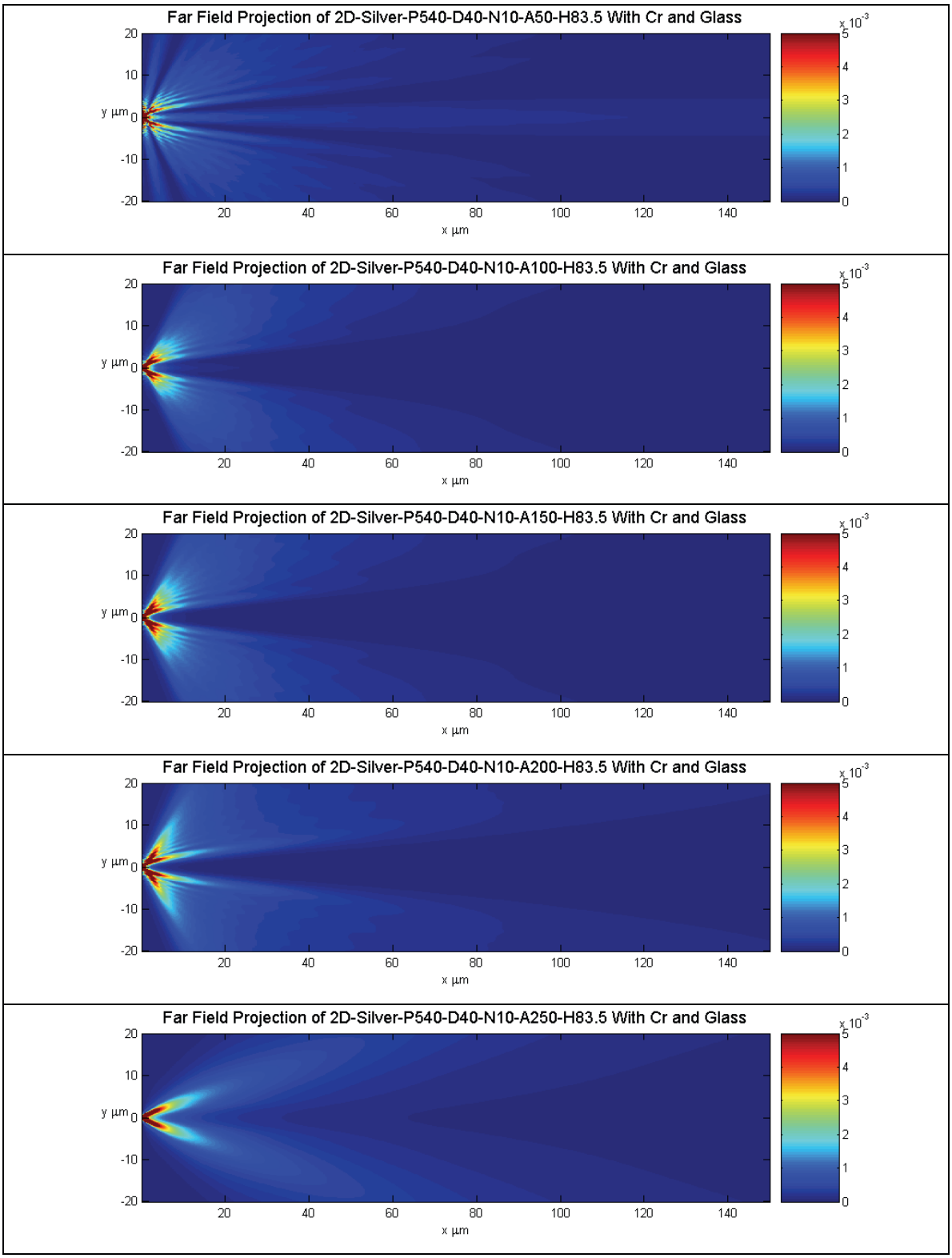

Figure 3-25: 2D intensity profile of nanoapertures in Silver with varying corrugation width. A* in the figure titles show the corrugation width.

Intensity vs Distance along x-axis

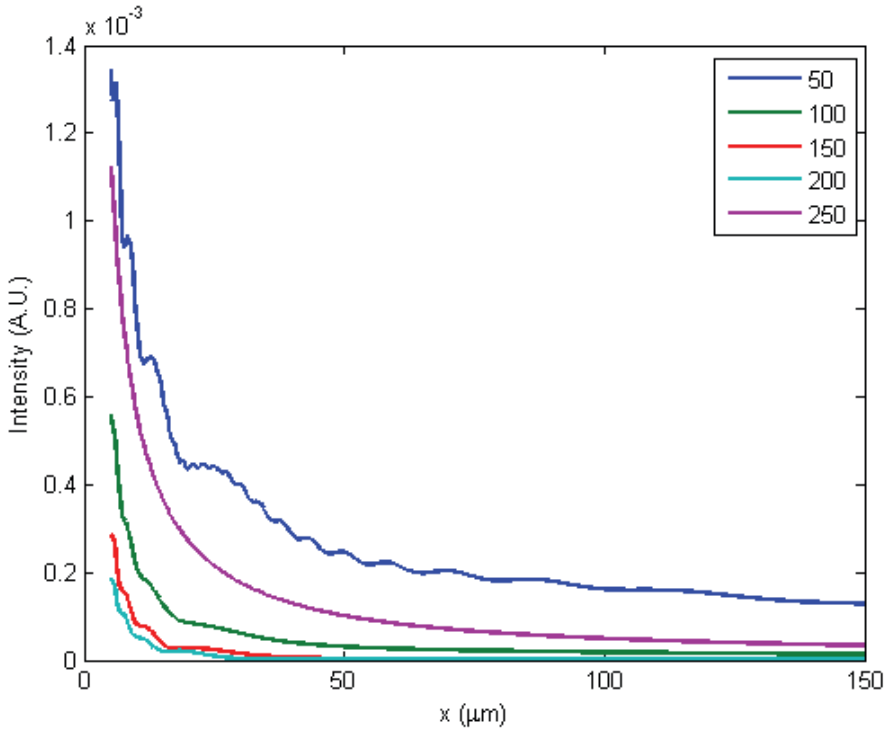

Cross-section intensity plot

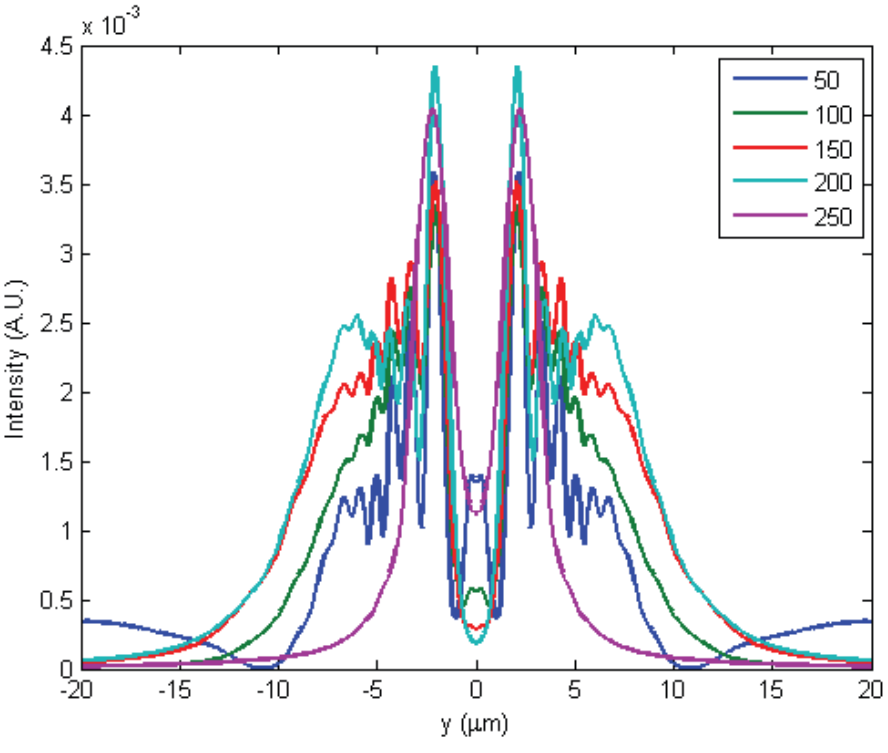

Figure 3-26: Top) Intensity plot of Silver along x-axis, and Bottom) corresponding cross-section intensity plot at the maxima of A.

3.2 Summary of the Simulations

The results from finite-difference time-domain simulations of nanoapertures with periodic corrugations in PEC, gold and silver were presented in this chapter. We were able to observe the effects when changes were made to the number of corrugations, corrugation period, corrugation depth, and corrugation width. In general, when the number of corrugations increased, beams became more apparent, on-axis or otherwise. Increasing corrugation period caused the beams to fan-out.

There were significant differences in the observed intensity profiles when different materials were used. We were able to attain a set of geometric parameters that allowed the formation of beams when using PEC. However, we were unable to attain a set of parameters that formed beams when using gold and silver.

As we were only able to attain beaming using PEC, we will use that set of geometric parameters for fabrication. Since it will be difficult to experiment with materials that very closely approximate PEC (i.e. superconductors), we will fabricate the nanoaperture in silver instead. This will help us confirm whether silver is a good approximation of PEC for surface plasmon assisted beaming applications. In the next chapter, we will discuss the fabrication of nanoaperture with periodic corrugations in silver.

4 FABRICATION OF NANOAPERTURES

The fabrication of subwavelength aperture and corrugation first requires the deposition of a metallic film on a substrate. The quality of the film is determined by a consistent thickness and optical density in the patterned region of the aperture. The nanostructures are then milled into the film using focused ion beam (FIB). For this research, we selected silver for easy comparison to other published results. The metal should be thick enough to be optically opaque. We chose 300nm as the film thickness as this is several times greater than the skin depth of silver for 532nm of light. The dimensions of the nanoaperture with periodic corrugations were determined from the results of the FDTD simulations (Chapter 3): number of corrugations = 10, corrugation periods = 500nm, aperture diameter and corrugation width = 40nm, corrugation depth = 83.5nm. The fabricated structures were investigated with Scanning Electron Microscopy (SEM).

4.1 Metallic Film Deposition

Silver was deposited by either sputtering or electron beam evaporation. Microscope glass slides were used as substrates. For sputtering, radio frequency generated plasma knocks atoms from a source target that contains the deposition material. The ejected atoms settle onto the substrate to form a thin film.

In electron beam evaporation, the deposition material was heated up to its vapour temperature by a laser. The evaporated metal condensed onto the substrate. The atoms ejected in laser evaporation tended to be less energetic compared to ones in sputtering. Atoms with lower energy are less mobile, resulting in formation of smaller grains. To obtain films with even smaller grains or to create an amorphous thin film, the glass substrate can be liquid nitrogen cooled to reduce the mobility of the deposited atoms even further.

4.2 Structure Milling

4.2.1 Focused Ion Beam

The nanoaperture and the surrounding corrugations were milled using Focused Ion Beam (FIB). Initially, the milling was performed by the author at the Nanoimaging Facility at 4D Labs at Simon Fraser University (SFU). The necessity of finer features required the higher resolution FIB at University of Western Ontario (UWO).

4.2.1.1 Fabrication at Simon Fraser University

The FIB system used was a FEI Strata DB 235. A black and white bitmap of the bulls-eye pattern was converted into a sequence of x-y coordinates for the ion beam to trace. Each coordinate is assigned a beam dwell time. For even dwell depth across the whole pattern, the coordinates were looped multiple times instead of a single pass [20][21]. The dwell depth is determined by the ion dosage, which is the total dwell time multiplied by the ion current. Several

combinations of ion current, dwell time, pattern density, and number of loops were tried to determine the best result for milling the 60nm corrugation depth.

The ion beam had a profile that is approximately Gaussian. It was required that the distance between coordinates was close enough so that the milled corrugations were continuous instead of distinguishable pits. The requirement was such that the distance between points was closer than the diameter at $1/e^2$ maximum current density [22].

The field of view of FEI Strata DB 235 at 10000x magnification was 14.42μm horizontal by 14.00μm vertical. It was separated into a 4096x4096 grid. The highest density pattern consisted of ion beam dwell points at every second coordinate. So the separation distance between dwell points was approximately 7nm. For the medium and low density pattern the separation distance was approximately 11nm and 18nm.

The corrugation area was 88.0μm^2. The ion beam current of 1pA and 50pA were used. (The 10pA and 30pA settings were unavailable.) The total dwell time for the entire pattern was 300sec and 30sec respectively.

Tracking and identification marks were also milled around the bulls-eye so that it can be located for alignment during testing. Figure 4-1 shows a scanning electron micrograph of a nanoaperture with periodic corrugations. Figure 4-2 shows other micrographs of nanoaperture fabricated at SFU.

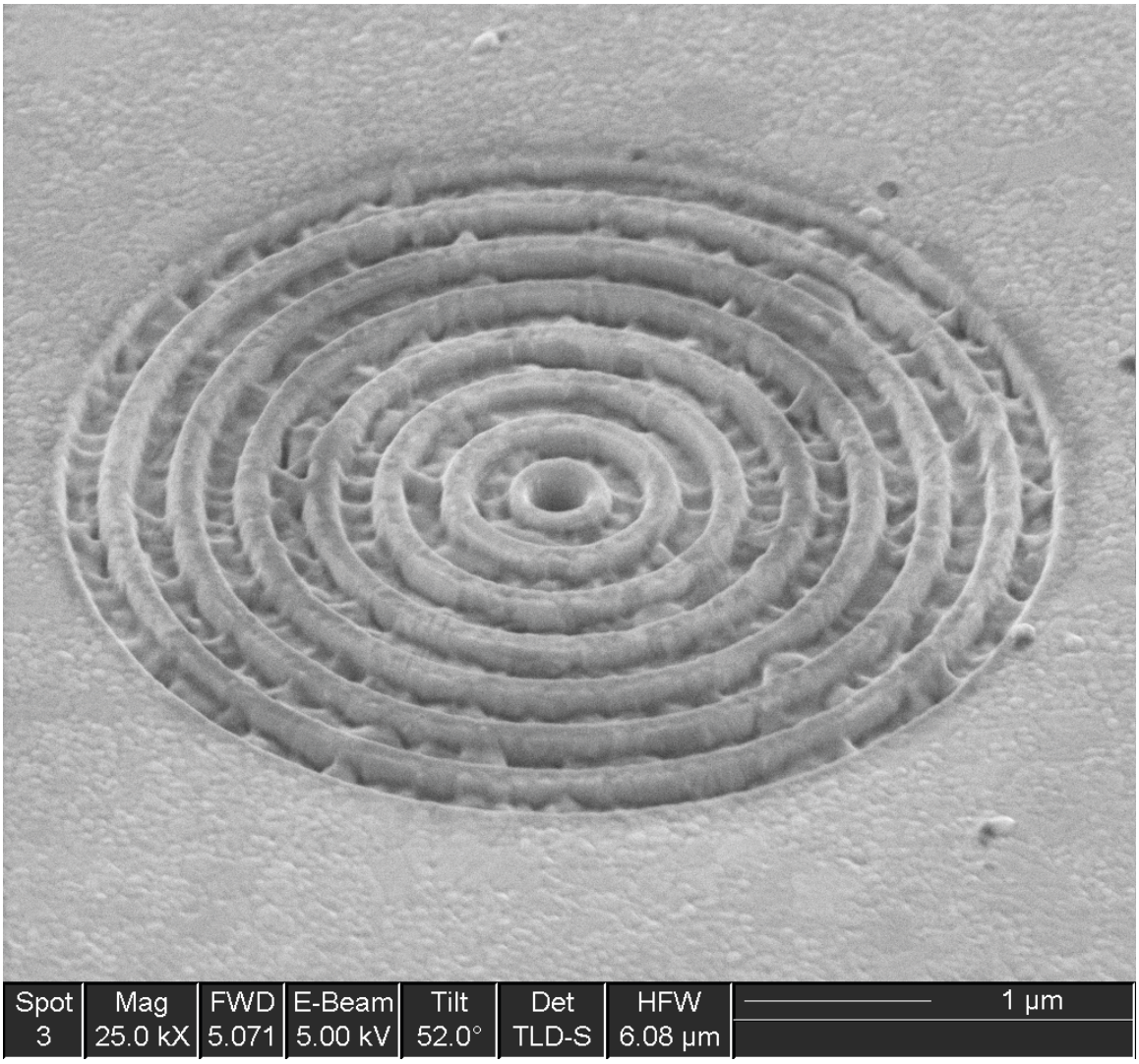

Figure 4-1: SEM image of milled bull's eye from SFU

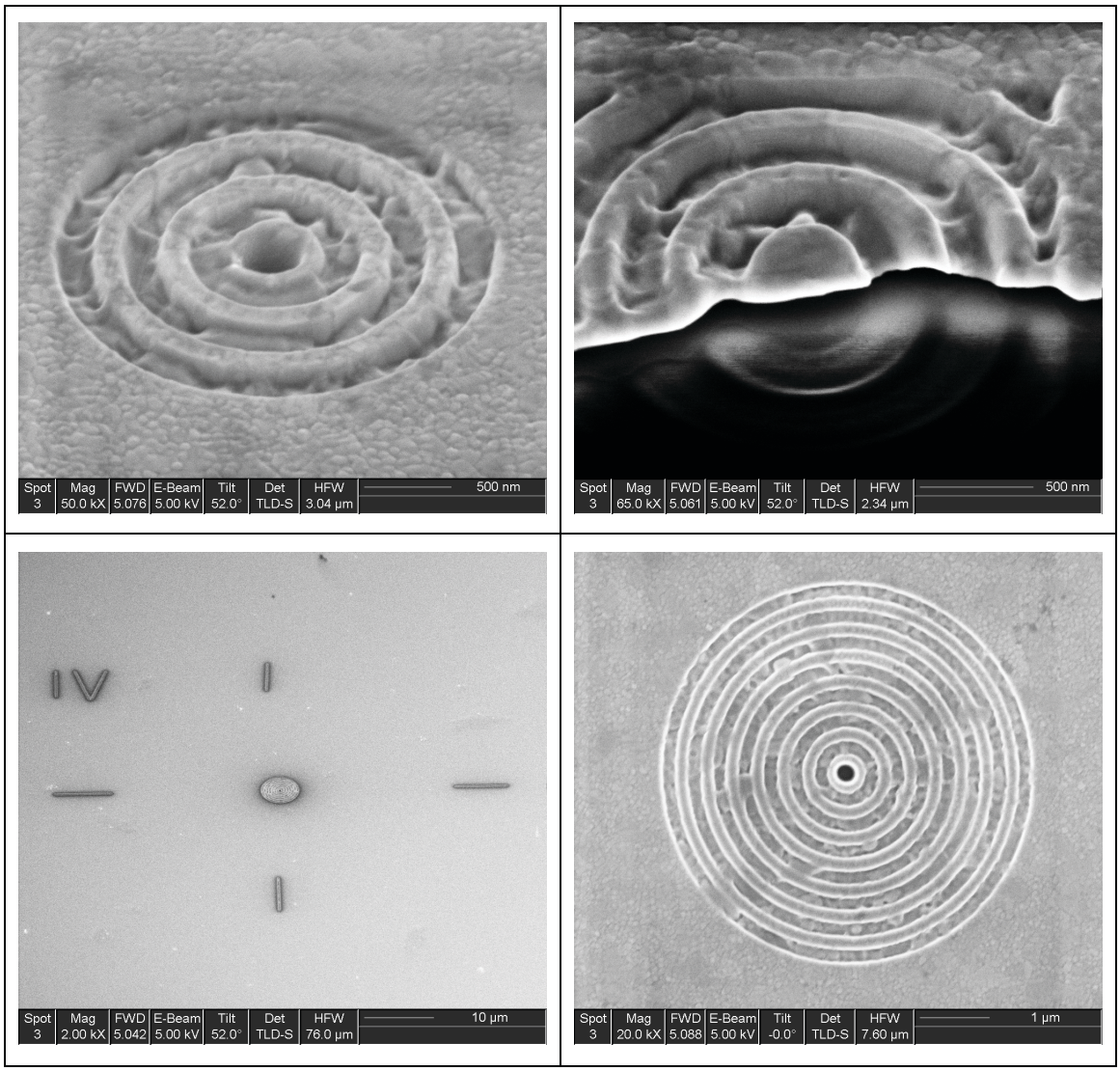

Figure 4-2: Various SEM images of trial nanoaperture milled at SFU. The micrograph in the bottom left shows the nanoaperture with the alignment marks.

4.2.1.2 Fabrication at University of Western Ontario

Requirements of feature size below 100nm were beyond the capability of the FIB at SFU. The services of the Nanofabrication Facility at UWO were procured. The FIB at this facility was a Leo 1540XE, capable of milling corrugations with widths of 40nm. The facility carried out the design instruction for the nanoaperture and corrugations. Figure 4-3 shows scanning electron micrographs of nanoapertures

that have been fabricated with the geometric parameters described at the start of the chapter. The bottom figure shows the cross-section exposing the groove depth.

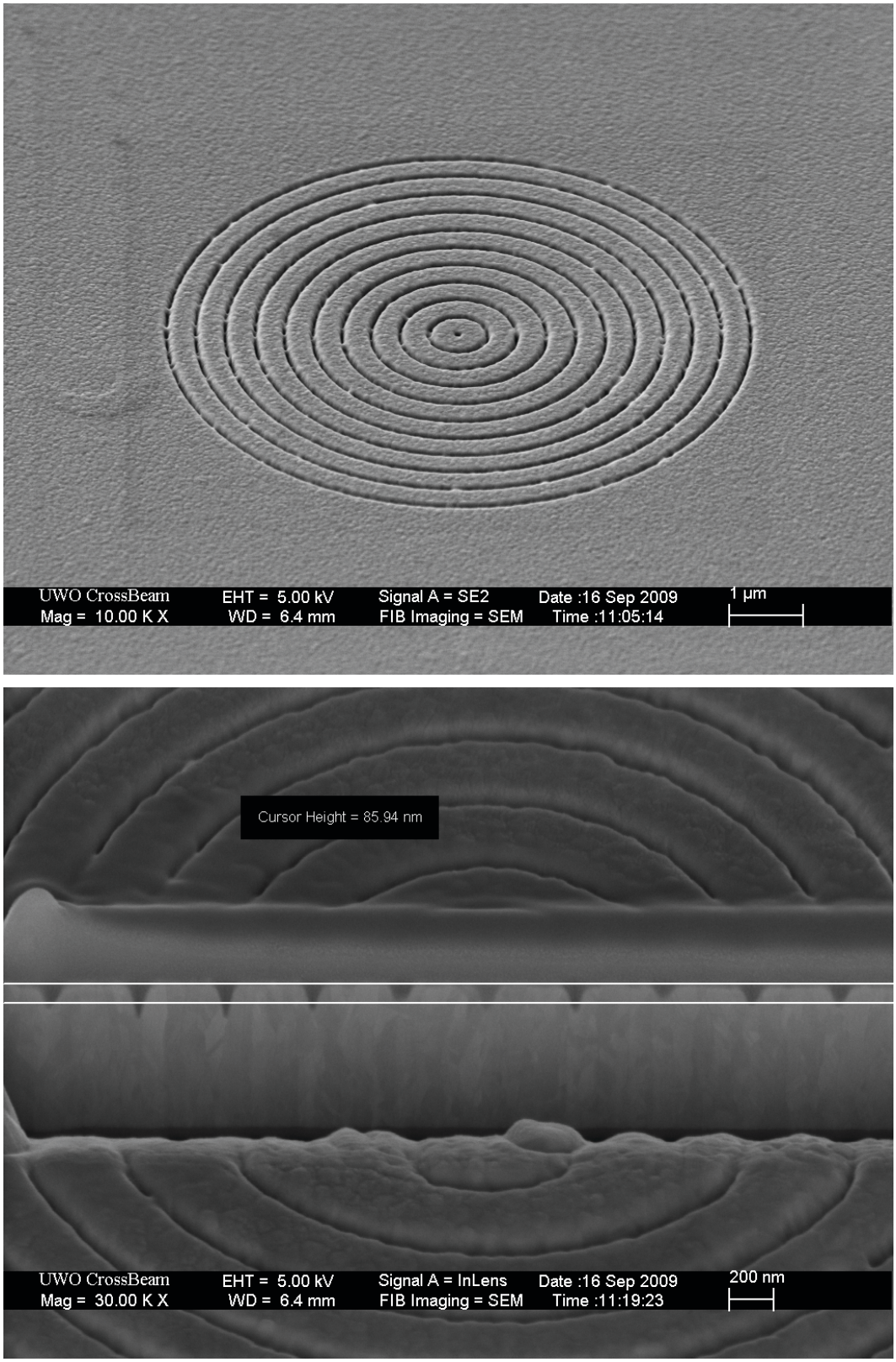

Figure 4-3: Milled bull's eye from UWO (top) and cross section (bottom).

4.3 Summary

The fabrication of nanostructures was discussed in this chapter. In the next chapter, the beam shaping performance of the UWO devices are characterized.

5 EXPERIMENTAL CHARACTERIZATION OF FABRICATED NANOAPERTURES

Following the fabrication of the nanoaperture structures presented in Chapter 4, the propagation of light and potential beaming was investigated. In this chapter, the light pattern is characterized using a classical knife edge experiment to investigate the beam formation.

5.1 Beam Profiling

5.1.1 Experimental Setup

To characterize the resultant beam width transmitted by the nanoaperture, the apparatus in Figure 5-1 was assembled to perform a standard knife edge experiment to measure the beam profile. A green frequency doubled neodymium-doped yttrium aluminium garnet (Nd:YAG) laser illuminated the back (unpatterned) surface of the metal, and light was detected on the other side. An opaque object with a sharply defined edge was slowly passed across the beam such that its beam profile could be determined. The chrome pattern on a US Air Force (USAF) Resolution Target was used as the knife edge. A 5μm layer photoresist spacer was deposited onto the surface of the resolution target to serve as a fixed distance spacer and to prevent scratching of the silver film in the region of the nanoaperture and surface corrugations. The resolution target was

mounted on a motorized 3-axis linear stage and the motion was controlled using LabView installed on a desktop PC through a Newport motion controller.

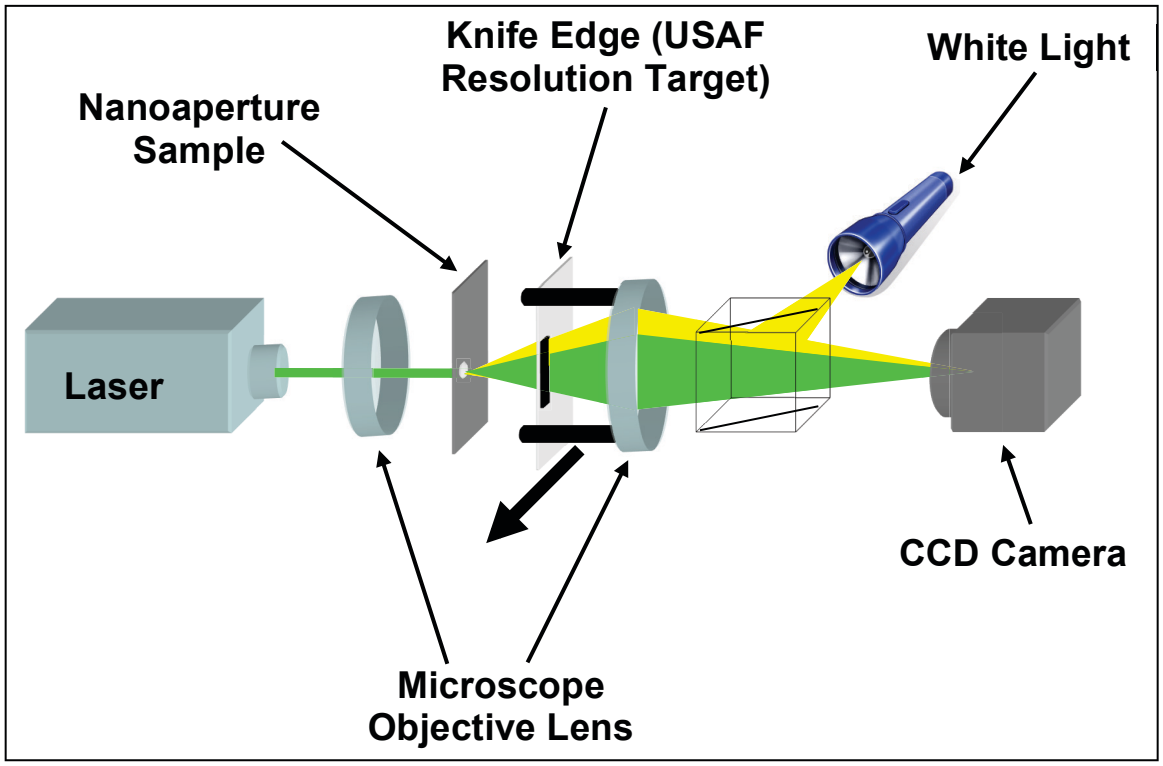

Figure 5-1: Schematic of knife edge experiment setup.

The detection optics consisted of a 20x microscope objective lens and a charge-coupled device (CCD) camera (Basler Scout scA1000-30fm) which were placed behind the resolution target. These were used to collect the light emanated from the aperture that passes the knife edge. The CCD camera was used to align the knife edge to the aperture, which was non-trivial given the small dimensions of the system. In order to record the light intensity with the CCD camera, the detector was moved out of focus, allowing the beam intensity to fill a large number of pixels without saturation. The measured light intensity was integrated

across the camera and sent to the PC where it was recorded using LabView. The measurement was synchronized with the stage motion.

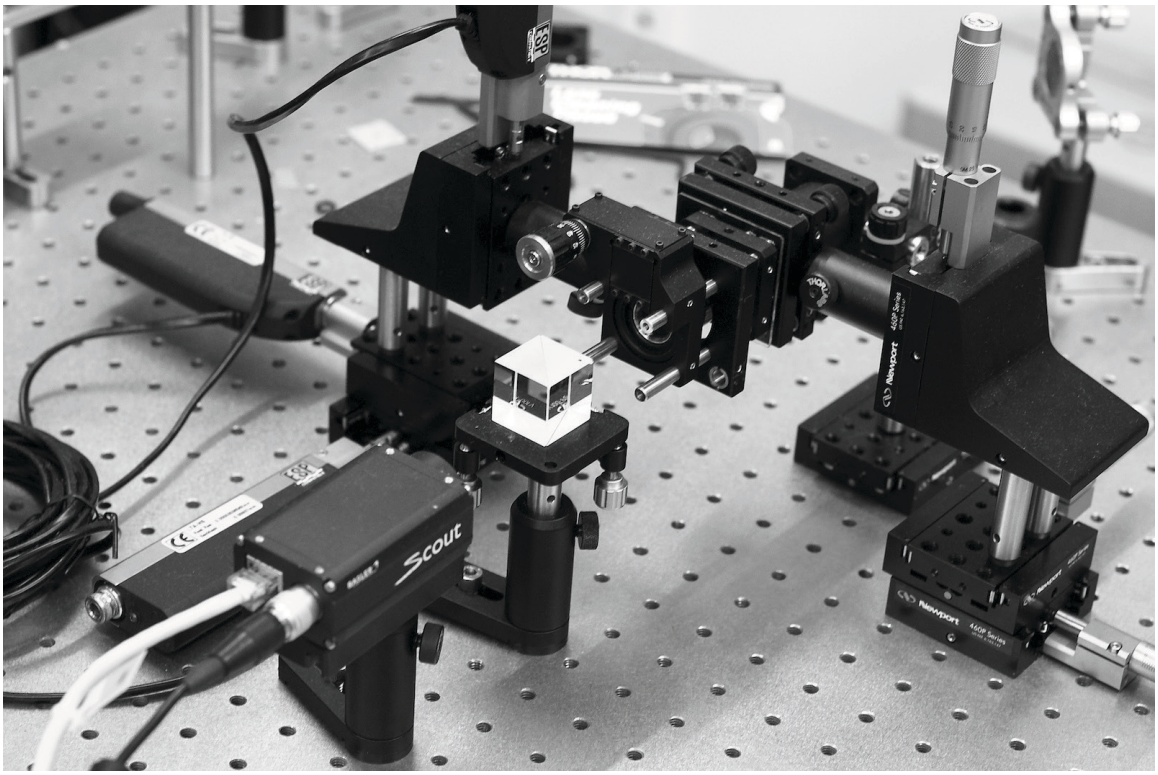

Figure 5-2: Photo showing the knife edge experimental setup

Figure 5-3 shows a schematic close-up of nanoaperture with the photoresist spacer and knife edge. The photoresist layer served as a known gap between the nanoaperture and knife edge when the resolution target is brought onto soft contact with the silver film. The spacer was formed by spinning Shipley 1827 onto the resolution target and baked at 100°C for 10 minutes. A well pattern was exposed into the photoresist around the knife edge using ultraviolet light on a mask aligner. The photoresist was then developed leaving the spacer surrounding the nanoaperture and corrugation, such that it does not interfere with

the transmitted light. The spacer thickness of 5μm was confirmed using a profilometer.

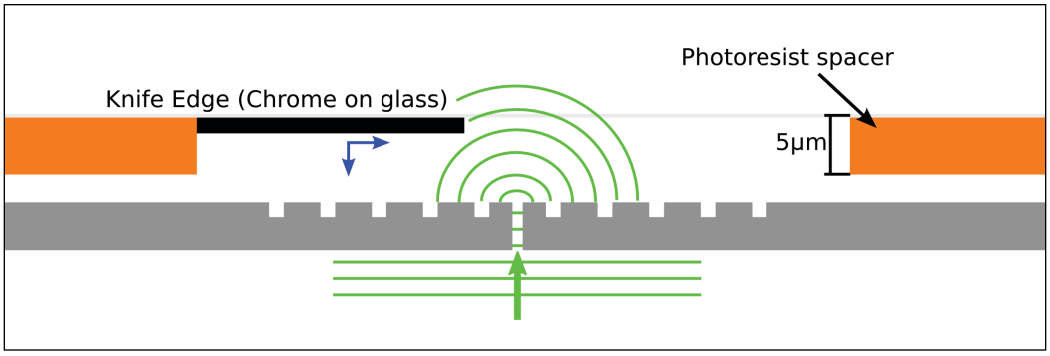

Figure 5-3: Schematic representation of the knife edge experiment. The photoresist on the knife edge provided a fixed distance spacer for the measurement.

5.1.2 Experimental Procedure

In order to measure the beam diameter, the stage supporting the knife edge was moved laterally in 0.2μm increments using the automated controller. It was moved a total of at least 200μm, adequate for the knife edge to traverse the full beam width. The knife edge was moved back and forth twice for a total of 4 measurements and the data were fit to the error function (*erf*). The stage was then moved along the optical axis such that beam diameter measurements could be repeated for the knife edge to nanoaperture separation distances of 5μm, 45μm, 85μm, 125μm, and 165μm. These experiments were performed for nanoapertures with 500nm and 512nm period corrugations. As well, a nanoaperture with no corrugations was characterized for comparison.

The data from each knife edge beam profiling measurement were fit to the parameterized function

$$f(x) = A \times erf\left(Bx - C\right) + D, \qquad \text{Eq. 5-1}$$

with parameters A, B, C, and D. *erf(x)* is the finite integral of the normalized Gaussian function. The $1/e^2$ radius is then equal to

$$r_{I=\frac{1}{e^2}} = \frac{1}{B\sqrt{2}}, \qquad \text{Eq. 5-2}$$

and the full-width half-max (FWHM) is

$$FWHM = \frac{2\sqrt{\ln 2}}{B}. \qquad \text{Eq. 5-3}$$

The beam width measurements from each of the profiles was averaged and reported. The average Gaussian fit to the beam shape at each axial position was then used to characterize the beam divergence. This can be represented as a linear plot of beam waist versus position.

5.1.3 Validation of Knife Edge Beam Profiling Experiment

To ensure that the experimental setup was measuring the beam width correctly, the nanoaperture was replaced by the cleaved end of a single mode fibre. The knife edge experiment described in the previous section was performed on the light exiting the fibre. The beam profile measurements at four different separation

distances are presented in Figure 5-4, and the divergence is recorded versus distance on Table 5-1. The measured beam width can then be used to calculate the diameter of the fibre core from Equation 5-4

$$w^2 = w_o^2\left(1+\left(\frac{\lambda z}{\pi w_o^2}\right)^2\right) \qquad \text{Eq. 5-4}$$

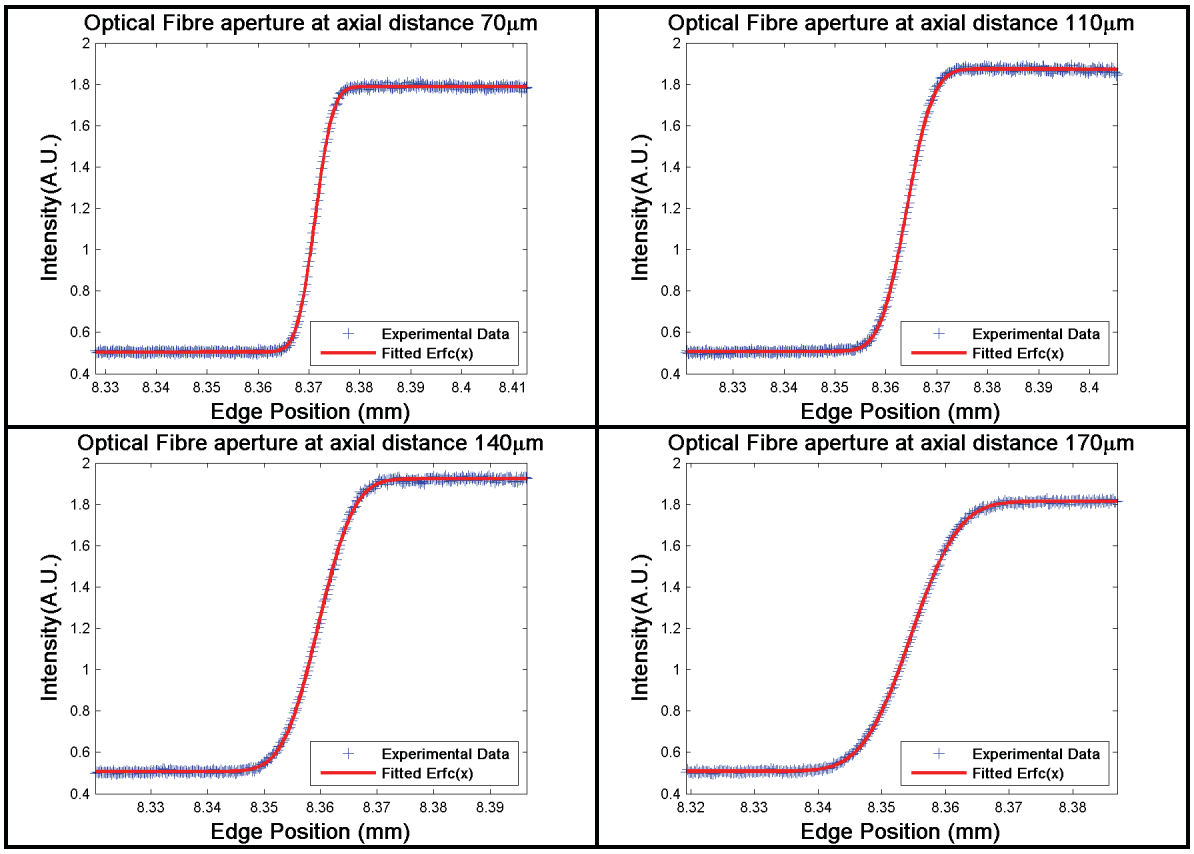

where w is the measured beam width, w_o is the fibre core diameter, z is the distance of the fibre opening to the knife edge, and λ is the wavelength of light used.

Figure 5-4: Knife edge measurements for light emitted from a single mode fibre.

The calculated core radius of 4.7±0.5μm matches the known dimensions of the fibre, confirming the validity of our knife edge experiment. Furthermore, this is similar in size to the diameter of the expected beams from the simulation in the PEC. The results indicate that our experimental setup has the resolution to detect beaming from the nanoapertures if it is present.

Table 5-1: Recorded measurements of the beam radius for light emitted from a fibre.

Knife Edge Separation Distance (μm)	$1/e^2$ Radius (μm)
70.2±0.2	5.5±0.5
110.2±0.2	8.2±0.5
140.2±0.2	9.9±0.5
170.2±0.2	11.9±0.5

5.2 Results from Fabricated Nanoapertures

The beam profiles were measured from the fabricated nanoapertures with no corrugations and corrugation periods of 500nm and 512nm. A representative beam profile from each axial position is presented in Figure 5-5, followed by the beam divergence for each aperture in Table 5-2 and Figure 5-6. By observation, the light from the nanoapertures was not collimated.

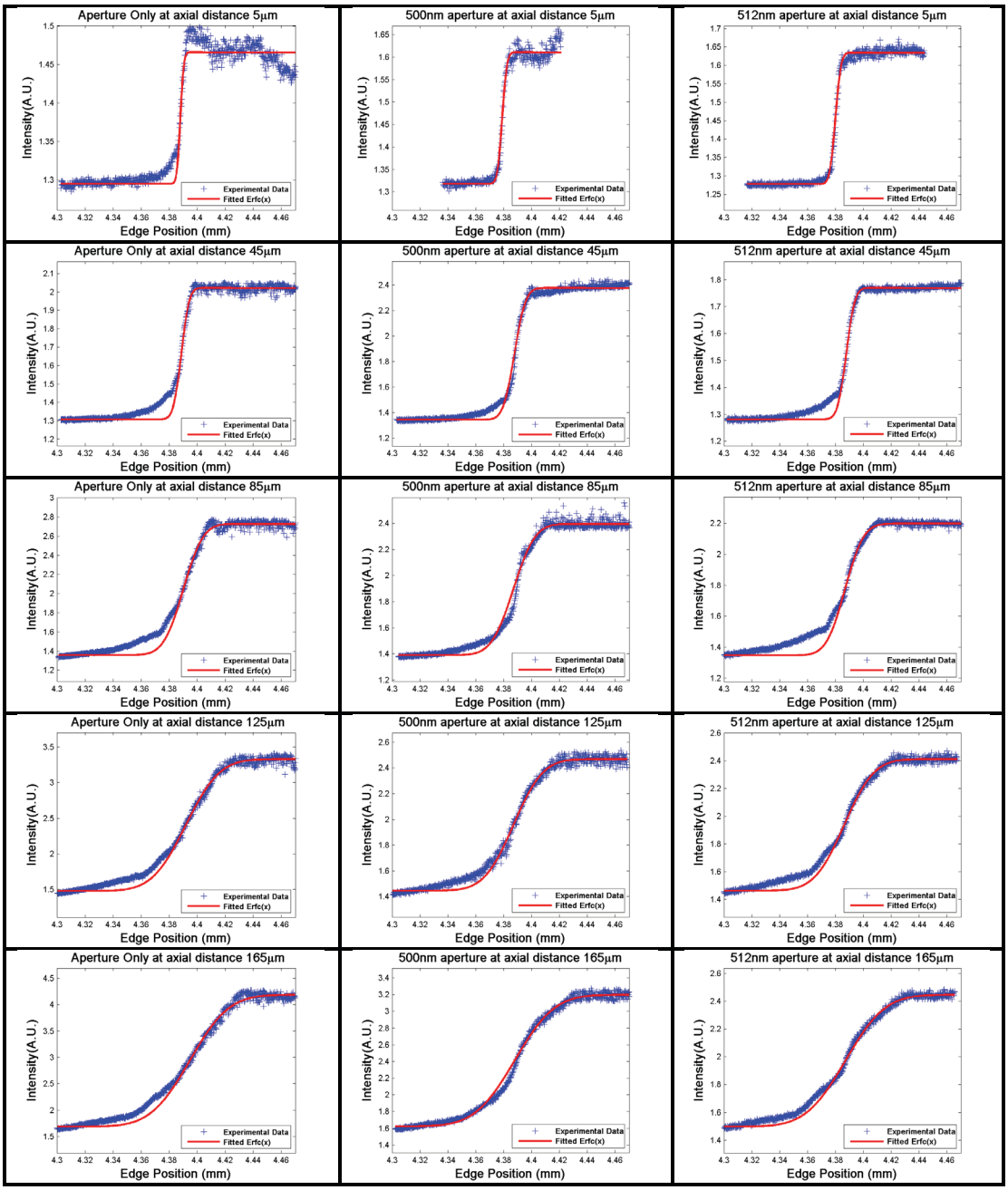

Figure 5-5: Knife edge measurements for aperture only, and aperture with 500nm and 512nm period corrugations.

Table 5-2: Measured $1/e^2$ radii beam width for the three condition of aperture with no corrugations, and with 500nm and 512nm period corrugations at varying distances.

Axial Distance	Hole Only	500nm	512nm
5μm	1.9±0.5μm	2.3±0.5μm	3.2±0.5μm
45μm	4.5±0.5μm	6.4±0.5μm	5.0±0.5μm
85μm	10.5±0.5μm	12.3±0.5μm	11.8±0.5μm
125μm	18.3±0.5μm	16.7±0.5μm	18.1±0.5μm
165μm	20.8±0.5μm	22.5±0.5μm	24.0±0.5μm

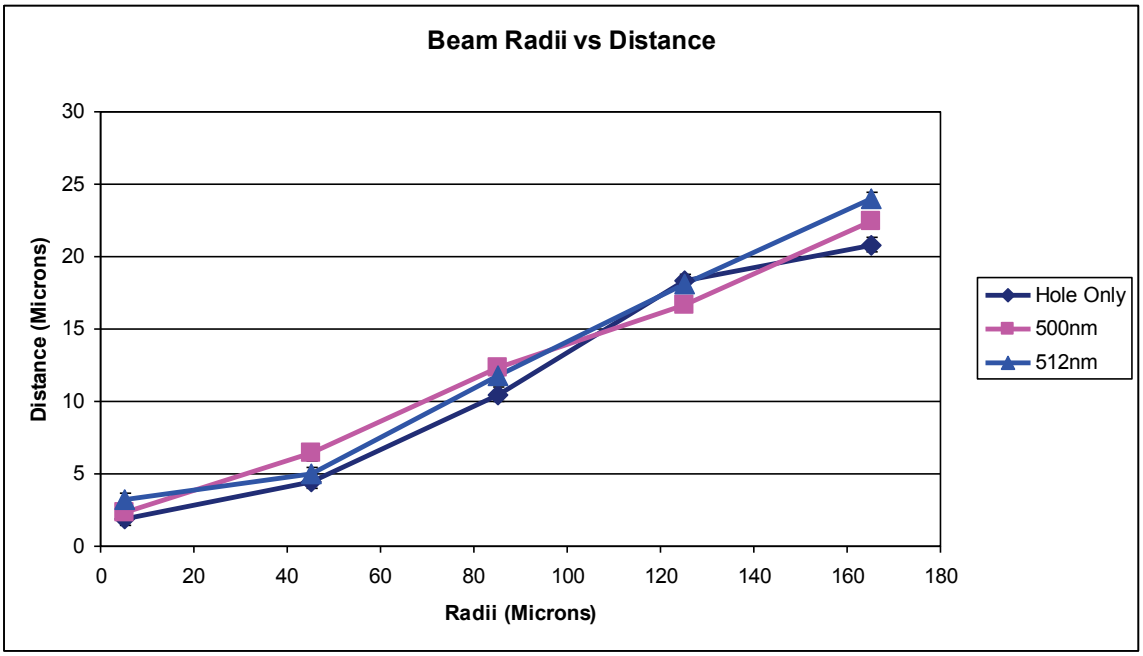

Figure 5-6: Graph of beam radii vs. distance.

Based on the results from Table 5-2 and Figure 5-6, the divergence of light from the nanoapertures was similar for all three geometries investigated. With these experiments, we were not able to confirm the beaming of light through the nanoaperture with corrugations.

5.3 Summary

The beam profiles from light emerging from the nanoapertures were measured using the knife edge technique. The knife edge beam profiling was validated using light emitted from a fibre. The measurements from the knife edge experiments did not detect formation of beaming light from the nanoapertures with corrugations. The measurements will be compared to the simulations of perfect conductors and real metals in the next chapter.

6 DISCUSSION

In Chapter 3 we investigated several geometric parameters for corrugations surrounding a nanoaperture and their effects on beaming using FDTD simulation. The barrier materials used were PEC, gold, and silver. In Chapter 5 we presented the results from the knife edge experiments to characterize the beams emanated from the nanoaperture we fabricated based on the simulations. In this chapter, we will compare the results from our simulations with those published in the literature. We will also discuss the experimental results and compare them to our FDTD simulations.

6.1 Comparing FDTD Simulations to Published Literature

The comparison of our FDTD simulations results of PEC to the analytical results in Garcia-Vidal [10] is straightforward for the exact same corrugation parameters. For the simulation with geometrical parameters A=40nm, H=83.5nm, P=500nm, and N=10, the results of our FDTD simulations in Figure 6-1 matched the analytical calculations presented in [10]. This suggests that the FDTD simulation provide a good complement to the analytical model for PEC.

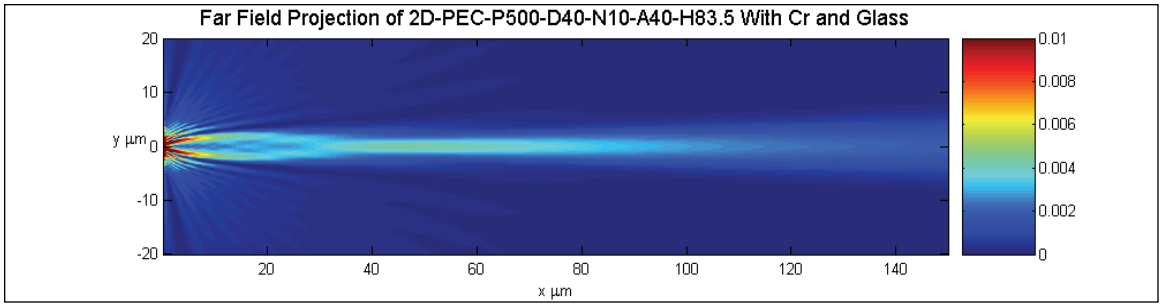

Figure 6-1: 2D intensity profile of nanoaperture with similar results as [10].

The FDTD simulation results from gold and silver with the same geometrical parameters as above did not show beaming corresponding to the simulations of PEC or the analytical results for PEC in [10]. This suggests that the PCM and PEC are inadequate in representing physical good conductors like gold and silver for surface plasmon assisted beam shaping. Neither PCM nor PEC take into account the finite conductance of real metals, which allows for the EM waves to penetrate into the surface of the metal. The interaction of these waves with the corrugations alters the behaviour of the EM waves when it recouples back to free space.

Our FDTD simulations of silver were similar to the FDTD simulations results attained from Wang et al. in [11]. Wang et al. compared their FDTD results to the QPCM and were able to attain good correlation. Neither our FDTD simulations of silver or Wang's analytical results display beaming using the same parameters as PEC. Furthermore we were unable to find a set of geometrical parameters that yielded beaming from our FDTD simulations of gold and silver using the bull's eye pattern.

6.2 Comparing FDTD Results to Experimental Results

In chapter 5 we performed a series of knife edge experiments to characterize the profile of transmitted beams from our nanoapertures fabricated in thin silver films. We were unable to observe any beaming from our apertures. This is consistent with the above discussion that PEC is a poor representation of real metals for surface plasmon assisted beaming.

Comparing the intensity profile from Figure 3-2 (simulation of no corrugations) and the graph in Figure 5-6 (knife edge measurement of beam width), we can see that our measurement of the divergence of light from an aperture without corrugations was narrower by a factor of ~6x than predicted by the simulations. There was also no observable difference between the three knife edge measurements (with and without corrugations) shown in Figure 5-6. The measured profile was significantly broader (10x at 80μm from the film) than expected if beaming had been achieved, indicating that a beam of light was not formed. Our knife edge experiment was only designed to confirm or reject if beaming was achieved. If the goal was to characterize the complex optical intensity pattern of strongly divergent light emanated from a nanoaperture with no corrugations, a completely different set of experiments would have been needed, such as using a collection-mode NSOM.

6.3 Summary

Our analysis showed that PCM is a poor model of real metals for surface plasmon assisted beam shaping. Furthermore, PEC is a poor substitute for real metals for this application. The results from our FDTD simulations of real metals are more consistent with the results shown from the QPCM. The knife edge experiment results showed there was no beaming from the nanoaperture with surrounding periodic corrugations, suggesting the FDTD simulations of real metals are correct. A qualitative comparison of the real beam profile and those predicted from FDTD simulations will require a different set of experiments using a collection-mode NSOM.

7 CONCLUSION AND FUTURE WORK

In this thesis, we furthered the investigations of beaming light through nanoapertures with surrounding periodic corrugations. Using the FDTD method, we performed a suite of simulations for PEC, gold, and silver. We examined how beaming is affected when varying different geometric parameters. We found that the transmitted beam profile is sensitive to the number of corrugations, corrugation width, corrugation period, and corrugation depth.

We compared the FDTD simulations results with the proposed analytical model published in the literature [10]. Our analysis found the results from FDTD simulations of PEC corresponded well with those from the PCM, while the FDTD simulations of real metals were consistent with those from QPCM.

Using the geometric parameters suggested from the FDTD simulations of PEC, we fabricated nanoapertures with periodic corrugations in silver using established nanofabrication techniques. The nanoaperture was then examined for the presence of beaming by performing a set of knife edge experiments. The experiments performed were unable to detect any appreciable difference of the beams from a bare nanoaperture from a nanoaperture with surrounding periodic corrugations. This further supports the argument that surface plasmon assisted beaming in real metals is poorly modeled by PCM and FDTD using PEC.

7.1 Contribution

This thesis furthered the work of previous research of models describing the mechanism of light beaming through nanoaperture surrounded by periodic corrugations. The Perfect Conductor Model and the Quasi-Perfect Conductor model proposed in the literature were investigated. Finite-difference time-domain simulations of light beaming through nanoaperture were performed using the Lumerical software. The Perfect Conductor Model proposed by Martin-Moreno was augmented with FDTD simulation results presented in this thesis of light beaming through nanoapertures in PEC, while the Quasi-Perfect Conductor Model proposed by Wang was augmented with FDTD simulation results of nanoaperture in real metals.

Nanoapertures were first fabricated at SFU using FIB. Subsequent nanoapertures requiring higher resolution FIB were fabricated at UWO. Light from fabricated nanoapertures were characterized by performing beam profile experiments. The measurements provide first-order results of light beaming through nanoapertures. The measurement results were compared with established models and FDTD simulation results presented in this thesis.

7.2 Future Work

To further the investigation of beaming light through nanoapertures using real metals as discussed in this thesis, one possible future direction is to modify the properties of the real metal film used in the experiment such that it closer

resembles the ideal properties of a perfect electrical conductor. A method to consider is to use metals or exotic materials that are different from the metals used in this thesis. Another possibility is to perform the experiment under cryogenic temperatures using superconductors. The results from these experiments can then be compared with the results from the FDTD simulations performed for PEC.

A second possible direction to further the investigation presented in this thesis is to build on the quasi-perfect conductor model for real metals. Our FDTD simulations only examined a limited set of geometric parameters of concentric corrugations with regular cross sections. Other geometries that lead to beaming may exist that are neither periodic nor rectangular. A greater understanding of the mechanism of beam shaping using surface plasmons would be needed to give an educated guess of the novel geometries and parameters. One method to further this understanding is to have the ability measure with very high accuracy the beam intensity profiles so that they can be compared with the results of the FDTD simulations for real metals. The knife-edge experiment discussed in this thesis was suitable for detecting beaming, but lacked the fine resolution to detect the complex intensity patterns that was seen in the results from the FDTD simulations. A collection near-field scanning optical microscope (NSOM) would be suitable for the accuracy required.

REFERENCES

[1] Greenfield Sluder and Joshua J. Nordberg, “Microscope Basics,” *Methods in Cell Biology*, 2007, vol. 81, pp. 1-10.

[2] P.J. Evennett and C. Hammond, “Microscopy Overview,” *Encyclopedia of Analytical Science 2nd Ed.*, Oxford: Elsevier Academic Press, 2005, pp. 32-41.

[3] Max Born and Emil Wolf, *Principle of Optics*, Cambridge: Cambridge University Press, 1999, p. 461.

[4] R. Dunn, “Near-Field Scanning Optical Microscopy,” *Chemical Reviews*, 1999, vol. 99, pp. 2891-2927.

[5] Y. Oshikane, T. Kataoka, M. Okuda, S. Hara, H. Inoue, and M. Nakano, "Observation of Nanostructure by Scanning Near-Field Optical Microscope with Small Sphere Probe," *Science and Technology of Advance Materials*, 2007, vol. 8, pp. 181-185.

[6] Xin Heng, David Erickson, L. Ryan Baugh, Zahid Yaqoob, Paul W. Sternberg, Demetri Psaltis, and Changhuei Yang, “Optofluidic Microscopy—A Method for Implementing a High Resolution Optical Microscope on a Chip,” *Lab Chip*, 2006, vol. 6, pp. 1274-1276.

[7] Xin Heng, Xiquan Cui, David W. Knapp, Jigang Wu, Zahid Yaqoob, Emily J. McDowell, Demetri Psaltis, and Changhuei Yang, “Characterization of Light Collection through a Subwavelength Aperture from a Point Source,” *Optics Express*, 2006, vol. 14, pp. 10410-10425.

[8] H.C. Lezec, A. Degiron, E. Devaux, R.A. Linke, L. Martin-Moreno, F.J. Garcia-Vidal, and T.W. Ebbesen, “Beaming Light from a Subwavelength Aperture,” *Science*, 2002, vol. 296, pp. 820-822.

[9] L. Martin-Moreno, F.J. Garcia-Vidal, H.J. Lezec, A. Degiron, and T.W. Ebbesen, “Theory of Highly Directional Emission from a Single Subwavelength Aperture Surrounded by Surface Corrugations,” *Physical Review Letters*, 2003, vol. 90, pp. 167401-167404.

[10] F.J. Garcia-Vidal, L. Martin-Moreno, H.J. Lezec, and T.W. Ebbesen, “Focusing Light with a Single Subwavelength Aperture flanked by Surface Corrugations,” *Applied Physics Letters*, 2003, vol. 83, pp. 4500-4502.

[11] Changtao Wang, Chunlei Du, and Xiangang Luo, “Refining the Model of Light Diffraction from a Subwavelength Slit Surrounded by Corrugations on a Metallic Film,” *Physical Review B*, 2006, vol. 74, pp. 245403-245410.

[12] William L. Barnes, Alain Dereux, and T.W. Ebbesen, “Surface Plasmon Subwavelength Optics,” *Nature*, 2003, vol. 424, pp. 824-830.

[13] E. Kretschmann and H. Raether, “Radiative Decay of Non-Radiative Surface Plasmons Excited by Light,” *Z. Naturforshung*, 1968, vol. 23A, pp. 2135-2136.

[14] F.J. Garcia-Vidal, H.J. Lezec, T.W. Ebbesen, and L. Martin-Moreno, “Multiple Paths to Enhance Optical Transmission through a Single Subwavelength Slit,” *Physical Review Letters*, 2003, vol. 90, pp. 213901-213904.

[15] Allen Taflove and Susan Hagness, *Computational Electrodynamics: The Finite-Difference Time-Domain Method 3rd Ed.*, Boston: Artech House, 2005.

[16] John David Jackson, *Classical Electrodynamics 3rd Ed.*, New Jersey: John Wiley & Sons Inc., 1998.

[17] Jean-Pierre Berenger, “A Perfectly Matched Layer for the Absorption of Electromagnetic Waves,” *Journal of Computational Physics*, 1994, vol. 114, pp. 185-200.

[18] K.R. Umashankar and A. Taflove, “A Novel Method to Analyze Electromagnetic Scattering of Complex Objects,” *IEEE Transactions on Electromagnetic Compatibility*, 1982, vol. 24, pp. 397-405.

[19] S.A. Schelkunoff, “Kirchhoof’s Formula, its Vector Analogue, and other Field Equivalence Theorems,” *Communications on Pure and Applied Mathematics*, 1951, vol. 4, pp. 43-59.

[20] H. Yamaguchi, A. Shimase, S. Haraichi, and T. Miyauchi, “Characteristics of Silicon Removal by Fine Focused Gallium Ion Beam,” *Journal of Vacuum Science Technology B*, 1985, vol. 3, pp. 71-74.

[21] H. Morimoto, Y. Sasaki, Y. Watakabe, and T. Kato, “Characteristics of Submicron Patterns Fabricated by Gallium Focused-Ion-Beam Sputtering,” *Journal of Applied Physics*, 1985, vol. 57, pp. 159-160.

[22] John Meingailis, “Focused Ion Beam Technology and Applications,” *Journal of Vacuum Science Technology B*, 1987, vol. 5, pp. 469-495.